Geoscience Frontiers 13 (2022) 101410

HOSTED BY

Contents lists available at ScienceDirect

Geoscience Frontiers

journal homepage: www.elsevier.com/locate/gsf

Research Paper

# Resolving impact volatilization and condensation from target rock mixing and hydrothermal overprinting within the Chicxulub impact structure

Thomas Déhais [a,b,*], Stepan M. Chernonozhkin [c], Pim Kaskes [a,b], Sietze J. de Graaff [a,b], Vinciane Debaille [b], Frank Vanhaecke [c], Philippe Claeys [a], Steven Goderis [a]

[a] Analytical, Environmental and Geo-Chemistry, Vrije Universiteit Brussel, Brussels, Belgium
[b] Laboratoire G-Time, Université Libre de Bruxelles, Brussels, Belgium
[c] Department of Chemistry, Atomic & Mass Spectrometry, Ghent University, Ghent, Belgium

ARTICLE INFO

*Article history:*
Received 6 January 2022
Revised 7 May 2022
Accepted 19 May 2022
Available online 23 May 2022
Handling Editor: S. Glorie

*Keywords:*
Chicxulub impact structure
Non-traditional stable isotopes
Impact volatilization
Impact condensation
Hydrothermal alteration
Target lithology mixing

ABSTRACT

This work presents isotopic data for the non-traditional isotope systems Fe, Cu, and Zn on a set of Chicxulub impactites and target lithologies with the aim of better documenting the dynamic processes taking place during hypervelocity impact events, as well as those affecting impact structures during the post-impact phase. The focus lies on material from the recent IODP-ICDP Expedition 364 Hole M0077A drill core obtained from the offshore Chicxulub peak ring. Two ejecta blanket samples from the UNAM 5 and 7 cores were used to compare the crater lithologies with those outside of the impact structure. The datasets of bulk Fe, Cu, and Zn isotope ratios are coupled with petrographic observations and bulk major and trace element compositions to disentangle equilibrium isotope fractionation effects from kinetic processes. The observed Fe and Cu isotopic signatures, with $\delta^{56/54}$Fe ranging from −0.95‰ to 0.58‰ and $\delta^{65/63}$Cu from −0.73‰ to 0.14‰, mostly reflect felsic, mafic, and carbonate target lithology mixing and secondary sulfide mineral formation, the latter associated to the extensive and long-lived (>$10^5$ years) hydrothermal system within Chicxulub structure. On the other hand, the stable Zn isotope ratios provide evidence for volatility-governed isotopic fractionation. The heavier Zn isotopic compositions observed for the uppermost part of the impactite sequence and a metamorphic clast ($\delta^{66/64}$Zn of up to 0.80‰ and 0.87‰, respectively) relative to most basement lithologies and impact melt rock units indicate partial vaporization of Zn, comparable to what has been observed for Cretaceous-Paleogene boundary layer sediments around the world, as well as for tektites from various strewn fields. In contrast to previous work, our data indicate that an isotopically light Zn reservoir ($\delta^{66/64}$Zn down to −0.49‰), of which the existence has previously been suggested based on mass balance considerations, may reside within the upper impact melt rock (UIM) unit. This observation is restricted to a few UIM samples only and cannot be extended to other target or impact melt rock units. Light isotopic signatures of moderately volatile elements in tektites and microtektites have previously been linked to (back-)condensation under distinct kinetic regimes. Although some of the signatures observed may have been partially overprinted during post-impact processes, our bulk data confirm impact volatilization and condensation of Zn, which may be even more pronounced at the microscale, with variable degrees of mixing between isotopically distinct reservoirs, not only at proximal to distal ejecta sites, but also within the lithologies associated with the Chicxulub impact crater.



## 1. Introduction

Hypervelocity impact events represent a fundamental geological process in the solar system with major consequences for the formation and the evolution of planetary surfaces and atmospheres (Dehant et al., 2019; Chernonozhkin et al., 2021). Large impact

* Corresponding author at: AMGC – Vrije Universiteit Brussel, Pleinlaan 2, 1050 Brussel, Belgium.
*E-mail address:* thomas.dehais@vub.be (T. Déhais).

https://doi.org/10.1016/j.gsf.2022.101410

events (>1 km in diameter projectiles) on Earth result in the formation of a rich variety of impactites, consisting of shocked target rocks, impact melt rocks, impact breccias and (distal) ejecta, which represent unique recorders of the extreme velocity, pressure and temperature conditions associated with impact events (Stöffler and Grieve, 2007). Several complex geological processes affect the structure and composition of these impactites during and/or after impact crater formation, such as impact volatilization and condensation, target rock mixing, and hydrothermal alteration. These processes are linked to the main stages of crater formation but are often not well constrained. During the first stage of contact and compression, shock waves produced by the impact lead to shock melting and vaporization of target rocks and the projectile itself. Then, the excavation phase corresponds to the formation of the transient cavity and the ejection of solid and melted target material. Subsequently, the crater modification stage causes the unstable transient crater to deform by inward and upward movements of fault-bounded blocks. In addition, the crater is rapidly filled by a mixture of impactite deposits by means of atmospheric and/or aqueous processes. Finally, within most impact structures, these three stages are followed by alteration processes linked to an impact-induced hydrothermal system, which can last for at least a couple of millions years after the impact (Kring et al., 2020).

To better understand and disentangle the different dynamic processes during large impact cratering events, various proximal impactites produced during or following the formation of the ~200-km-diameter Chicxulub impact structure on the Yucatán peninsula, Mexico (Fig. 1) were examined petrographically, geochemically, and isotopically. Here, our main focus lies on the variations of the isotopic ratios of the non-traditional stable isotopic systems Fe, Cu and Zn in Chicxulub drill core samples. The difference in volatility between Fe, Cu, and Zn is expressed by their 50% condensation temperature ($T_{50}$). The $T_{50}$ is the calculated temperature for which half of an element's mass is condensed from a cooling gas of solar composition at equilibrium and at a nebular total pressure ($10^{-4}$ bar; Wood et al., 2019). The three elements selected for isotopic analysis display different geochemical behavior: Fe is refractory ($T_{50}$ = 1338 K) and siderophile, Cu is moderately volatile ($T_{50}$ = 1034 K) and chalcophile, while Zn is highly volatile ($T_{50}$ = 704 K) and lithophile (Wood et al., 2019). Zinc has also been classified as slightly chalcophile (Barnes, 2016). The distinct geochemical properties and behavior of Fe, Cu, and Zn are exploited here to untangle a range of processes taking place during impact cratering events. Previous studies have demonstrated the potential of isotopic proxies to trace impact evaporation, condensation, and mixing of the target components by applying isotopic analysis of Li, Zn and Cu (Rodovská et al., 2016, 2017), Sn (Creech et al., 2019), Pb (Ackerman et al., 2020), K (Magna et al., 2021), and Fe (Chernonozhkin et al., 2021) to (micro)tektites. In addition, stable Zn isotope ratios were successfully used to characterize melt sheet material from the Sudbury impact structure in Canada (Kamber and Schoenberg, 2020). Recently, Mathur et al. (2021) performed Zn isotopic analysis of K-Pg boundary sediments, revealing heavier Zn isotopic compositions and lower Zn concentrations within the K-Pg boundary claystone relative to the surrounding sedimentary rocks. These results provide clear evidence of volatilization taking place during the Chicxulub impact event, but additional data on the source region and materials are needed to further refine this interpretation. Hence, by applying several non-traditional isotopic proxies to a wide range of proximal impactites from Chicxulub we provide a unique perspective on impact volatilization close to a large impact structure. Careful integration of isotopic data with bulk and *in situ* geochemical data, together with petrographic observations, can uniquely resolve the effects of volatilization

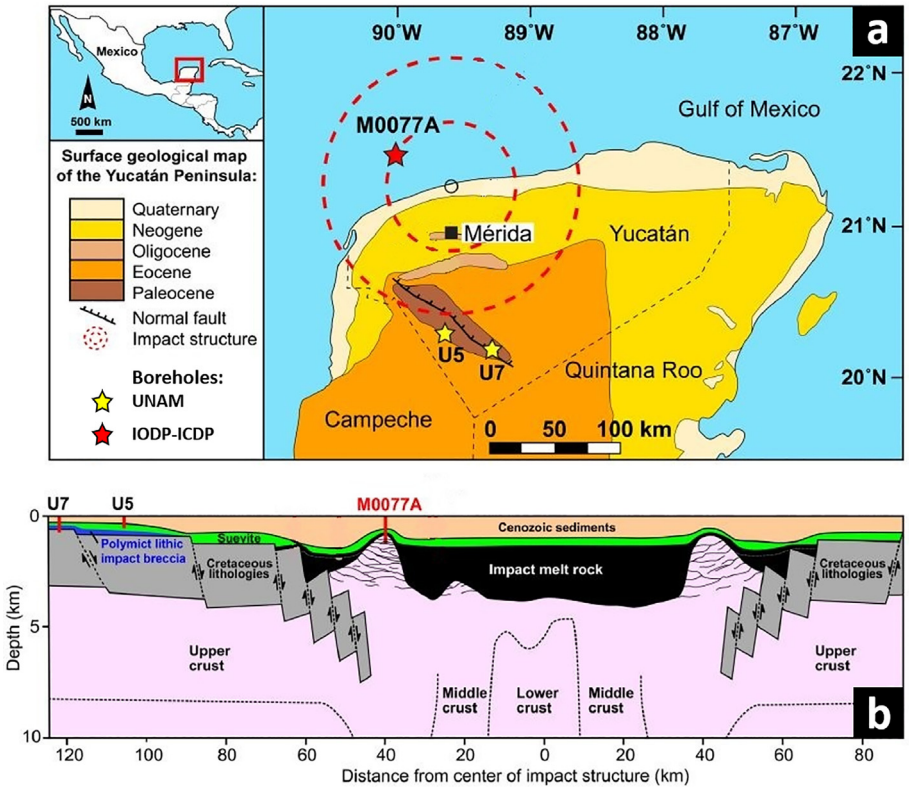


**Fig. 1.** (a) Simplified geological map of the Yucatán Peninsula (Mexico) with the locations of the Chicxulub impact structure, its peak ring, and the M0077A, UNAM 5 (U5) and UNAM 7 (U7) boreholes (adapted from Kaskes et al., 2022). (b) Schematic geological cross-section of the Chicxulub impact structure showing the interpreted sequence from crustal rock to Cenozoic sediments and the locations of the drill cores used in this study (adapted from Kaskes et al., 2022).

and condensation from complex mixing of distinct target lithologies and post-impact hydrothermal alteration.

## 2. Geological setting

The Chicxulub impact structure on the Yucatán peninsula in Mexico formed ~66 Ma ago (Sprain et al., 2018) by the hypervelocity impact of a ~12 km asteroid (Collins et al., 2020) into a complex target composed of ~3 km thick layer of Mesozoic carbonate- and sulfate-rich sedimentary rocks overlying a granitoid basement (Morgan et al., 2016). The Chicxulub impact event is associated with a globally distributed ejecta layer, enriched in iridium, impact spherules, some of which contain Ni-rich spinel crystals, and shocked mineral grains, all of which have been used to link it to the extinction of the non-avian dinosaurs at the Cretaceous-Paleogene (K-Pg) boundary (e.g., Swisher et al., 1992; Smit, 1999; Schulte et al., 2010; Goderis et al., 2021). The Chicxulub impact structure represents one of the best-preserved large complex impact structures on Earth (Fig. 1; Hildebrand et al., 1991; Gulick et al., 2008) and is the only known terrestrial impact structure preserving a topographic peak ring (Morgan et al., 1997, 2016). This topographic peak ring was jointly drilled in 2016 by the International Ocean Discovery Program (IODP) and the International Continental Scientific Drilling Program (ICDP) during Expedition 364 at Site M0077A (WGS84 coordinates: 21.45° N, 89.95° W; Morgan et al., 2016; Fig. 1). Drill core material from this site constitutes the main focus of this study. From bottom to top, the Hole M0077A drill core is composed of ~590 m of granitoid basement intruded by pre-impact dikes and an impact melt-bearing unit, ~130 m of impact melt rock and suevite (polymict impact-melt bearing breccia), and ~110 m of Paleogene sediments (Morgan et al., 2017). These lithologies were emplaced during a complex series of dynamic processes, such as by melt injection during peak ring formation and melt emplacement on top of the peak ring in the modification stage, followed by deposition linked to a forceful ocean resurge within the crater, seiche movements, returning tsunami waves and atmospheric fallout of ejected material (Morgan et al., 2016; Goderis et al., 2021; de Graaff et al., 2022; Kaskes et al., 2022).

The main lithological units of the Hole M0077A drill core have petrographically been described in several studies. The basement (747.02–1334.68 m below sea floor; mbsf) is composed of several crystalline pre-impact lithologies. The most abundant lithology within the Hole M0077A drill core is represented by the granitoids. The granitoids are interspersed by pre-impact magmatic dikes, such as dolerite, felsite, and dacite. As the dolerite dikes are by far the most abundant type, other pre-impact dike lithologies have not been included in this study. We refer to de Graaff et al. (2022) and Feignon et al. (2021) for in-depth petrographic descriptions of the crystalline pre-impact lithologies.

The lower impact melt–bearing rock (LIMB) unit occurs within the lowermost part of the basement sampled by the Hole M0077A drill core. It contains altered impact melt rock fragments similar to the upper melt rock and basement-derived material ranging from single crystals (<1 mm) to clasts (up to few cm; de Graaff et al., 2022). The LIMB unit is interpreted to represent impact melt rock injected into the crystalline basement during the compression/excavation stage of the impact cratering process.

The upper impact melt rock (UIM) unit (715.60–747.02 mbsf; upper limit redefined by Kaskes et al., 2022) contains two distinct lithological components, clast-bearing black impact melt rock and green schlieren (de Graaff et al., 2022). The former contains diverse clast types, which represent the different basement lithologies and their abundances, embedded in a compositionally varying matrix. Green schlieren, irregular streaks of mostly sparry calcite and Fe-bearing phyloosilicates that differ from the surrounding rock in texture and composition, mainly occur between 721.61 and 737.56 mbsf and are pervasive throughout the clast-bearing black impact melt rock. The macroscopic texture of these two UIM components range from brecciated with angular black impact melt rock clasts to features of mingling (de Graaff et al., 2022). The composition of the UIM unit implies the entrainment of carbonate components and is interpreted to have stayed at the surface during crater development. Its formation was not finalized until the modification stage, when carbonate material would have reentered the crater (de Graaff et al., 2022).

The suevite (617.33–715.60 mbsf) is a polymict impact-melt bearing breccia with a particulate, fine-grained groundmass (mostly clastic carbonate and aluminosilicate). Diverse materials are embedded within the groundmass, such as target mineral and rock clasts, and abundant angular impact melt particles (Kaskes et al., 2022). These particles are altered and mainly angular without phenocrysts (formerly vitric), whereas other particles present a plagioclase microlite-dominated matrix (microcrystalline) with felsic basement clasts (Kaskes et al., 2022). The target rock clasts are less abundant than impact melt fragments and are mostly carbonate and felsic basement clasts (granitoid and gneiss). Only few mafic basement clasts (such as dolerite) can be found, mainly in the lower half of the suevite sequence (Kaskes et al., 2022). All sections constituting the suevite unit display evidence of post-impact hydrothermal alteration (Kring et al., 2020). The suevite section has been divided in three subunits by Kaskes et al. (2022). The lowermost non-graded suevite (710.01–715.60 mbsf) is characterized by a poorly sorted texture and a clastic groundmass. The overlying graded suevite (620.88–710.01 mbsf) is characterized by a wide range of target rock clasts and a fining-upward and increasingly well-sorted upward trend (Kaskes et al., 2022). In contrast to the previous subunits with a randomly organized clast texture, the bedded suevite (617.33–620.88 mbsf) is characterized by a clear bedding and imbrication of clasts. It contains abundant isolated planktic and benthic Cretaceous foraminifera, which are associated with calcite cement and some pyrite minerals (Kaskes et al., 2022). The deposition of these suevite subunits has been interpreted to have happened within 1 day after impact (Gulick et al., 2019) and results from the initial seawater ingress and melt-water interactions at the base, followed by a full ocean resurge in the crater that transitioned into seiche movements and a returning tsunami at the top of the sequence (Kaskes et al., 2022).

The transitional unit (616.54–617.33 mbsf) is a micritic bedded unit that fines upwards from pebble to fine sand size grains with abundant sulfide levels (Bralower et al., 2020; Whalen et al., 2020). The coarse grains are mainly altered impact glass fragments (phyllosilicate minerals), carbonate intraclasts, composite and coated grains, crystalline calcite grains, foraminifera, and other bioclasts (Whalen et al., 2020). The uppermost part of this unit displays the presence of bioturbations (burrows; Whalen et al., 2020), while the lower part exhibits sedimentary structures such as dewatering pipes or fluid and vapor channels that are associated with the hydrothermal system (Kring et al., 2020). Both the top and bottom of the transitional unit contain charcoal grains associated with sulfide mineralizations and the lowermost part also displays several other distinct pyrite layers (Bralower et al., 2020). Sulfides throughout the Paleogene marlstone, the transitional unit, and uppermost suevite are mainly pyrites ($FeS_2$), but include chalcopyrite ($CuFeS_2$) and sphalerite or wurtzite (ZnS; Goderis et al., 2021). In addition, some bravoite grains (small Ni-Co-rich sulfides, $(Fe,Ni,Co)S_2$) are present around the transition between the transitional unit and the suevite (Goderis et al., 2021).

The Paleogene sediments (505.70–616.54 mbsf) are composed of post-impact pelagic white limestone overlaying 3 cm thick

green marlstone (Bralower et al., 2020). The latter layer is characterized by a positive iridium anomaly of ~1 ppb (Goderis et al., 2021). It also contains charcoal grains (Bralower et al., 2020) and a diffuse pyritic interval (Gulick et al., 2019) with two thin concentrated layers and several cm-sized pyrite nodules (Goderis et al., 2021).

The samples from the Universidad Nacional Autónoma de México (UNAM) selected in this study are from the suevite-like polymict impact breccia unit containing evaporite clasts from the former carbonate platform overlaying the basement lithologies before the impact (Urrutia-Fucugauchi et al., 1996, 2014). This unit is a part of the ejecta blanket, and both UNAM-5 (U5) and UNAM-7 (U7) drill cores have been retrieved outside of the Chicxulub impact structure in the mid-1990 s, at respectively 110 km and 127 km away from the geometric crater center towards the South (Urrutia-Fucugauchi et al., 1996, 2008, 2014; WGS84 coordinates: 20.34° N, 89.66° W and 20.20° N, 89.25° W, respectively; Fig. 1). The suevite-like polymict impact breccia unit is 172-m thick within the U5 drill core and 126-m thick within the U7 drill core. This unit contains abundant carbonate clasts (including evaporite), impact melt fragments, and felsic basement material (Rebolledo-Vieyra et al., 2000).

## 3. Materials and methods

### 3.1. Sample selection

Bulk rock samples (~20 $cm^3$) were collected during three different sampling campaigns: the post-cruise sampling party at the MARUM-Bremen Core Repository in Germany (September 2016), an additional sampling campaign at MARUM (December 2017), and the final sampling campaign at the College Station-Texas Core Repository in the USA (October 2018). In total, 37 samples from the Chicxulub impact structure were selected and included in this work (Table 1). Thirty-five of these samples originate from the Hole M0077A drill core and have been characterized in terms of their petrography and geochemistry (major and trace element compositions) during previous studies (Feignon et al., 2021; de Graaff et al., 2022; Kaskes et al., 2022). As such, sample nomenclature used in this study as Core#_Section#_Top(cm)_Bottom(cm) is identical to that applied in de Graaff et al. (2022) and Kaskes et al. (2022). This naming system precisely denotes the intervals sampled and analyzed, where the centimeter notation corresponds to the distance from the top of the core section. Sample names associated to their lithological units and their depth are summarized in Table 1.

During sampling, particular attention was paid to intervals representative of distinct lithological units and specific formational or depositional processes. One sample was selected from the Paleogene (post-impact) sediments at 616.52 mbsf. This sample is from the top part of the iridium layer found within the Chicxulub impact structure (Goderis et al., 2021). Four samples were selected from the transitional unit. Fourteen samples derived from the suevite unit. The three suevite subunits described and defined by Kaskes et al. (2022) were sampled as follows: three samples were taken from the bedded suevite unit, ten samples from the graded suevite unit, and one sample from the non-graded suevite unit. Six samples were selected from the UIM unit. These samples range from macroscopically homogeneous black clast-poor impact melt rock (91_1_44_46, 93_1_19_21, and 95_1_52_54) to dark green impact melt rock with schlieren containing angular black melt fragments (87_2_73_75 mostly dark green, 87_2_56_58 and 89_1_57_59 mix of black and dark green). For a representative sampling of the target lithologies, ten samples were selected from the lower core intervals, including four granitoids, three dolerite dikes, one metamorphic clast, and two LIMB samples.

To complement the sampled units from within the Chicxulub impact structure, two samples of UNAM drill cores were analyzed. One originates from the U5 core at a depth of 500.55–500.65 m and the other one from the U7 core at a depth of 267.40–267.50 m. These two samples have been selected to compare with the isotopic signatures within the impact structure (Hole M0077A drill core), which are the main focus of this study. The number of samples available from UNAM drill cores is extremely limited and it is impossible to obtain new ones, which is why only two samples from U5 and U7 have been included in this study.

### 3.2. Petrography

Thirty thin sections were examined under plane-polarized light (PPL) and cross-polarized light (XPL) using a Zeiss (Carl Zeiss GmbH, Jena, Germany) Axioscope 5 TL/RL polarizing microscope equipped with a Zeiss Axiocam 208 camera at the Vrije Universiteit Brussel, Belgium (VUB). Micro-X-Ray Fluorescence (μXRF) element maps obtained in previous studies of the IODP-ICDP Exp. 364 drill core (Goderis et al., 2021; Kaskes et al., 2021, 2022) were used to locate potential Fe, Cu, and Zn-bearing mineral phases. Four representative thin sections throughout the drill core (40_2_0_3, 59_2_74_76, 95_1_52_54, and 293_1_49_52) were analyzed in more detail using a JEOL JSM-IT300 (JEOL Ltd., Tokyo, Japan) scanning electron microscope equipped with an energy-dispersive X-ray spectrometer (SEM-EDS) at the VUB. Potential Fe, Cu and Zn mineral carriers were characterized by backscattered electron images and qualitative EDS spot analyses using an acceleration voltage of 15.0 kV and a pixel dwell time of 2 min.

### 3.3. Fe, Cu and Zn isotopic analysis

All geochemical data in this study were obtained for homogenized powdered samples that were prepared at the Vrije Universiteit Brussel (VUB) using an agate mortar and pestle, and a Fritsch Pulverisette 5 agate ball mill, as described by de Graaff et al. (2022). Major and trace element compositions of the two UNAM samples were obtained at the Laboratoire G-Time at Université Libre de Bruxelles (ULB) using inductively coupled plasma-optical emission mass spectrometry (ICP-OES) and inductively coupled plasma–mass spectrometry (ICP-MS), respectively, following the same methods as described by de Graaff et al. (2022). All major element data in this study are recalculated and normalized to 100% on a volatile-free basis, with iron expressed as total ferric iron ($Fe_2O_3^T$). All ICP-OES and ICP-MS results are reported in Supplementary Data Table S1.

The preparation for Fe, Cu, and Zn isotopic analysis was performed under a class-100 laminar flow hood in a class-1000 clean lab at the ULB. The homogenized powders (~50–150 mg) were taken from the same bulk samples as those prepared by de Graaff et al. (2022) for major and trace element concentration measurements. The samples were dissolved on a hotplate in Savillex™ screw-top beakers at 110 °C successively using 4 mL of concentrated HF-$HNO_3$ (1:3), 4 mL of 6 M HCl, and 1 mL of 6 M HCl. The solution was evaporated in-between the different steps and the last 1 mL solution was loaded onto the chromatographic column. Sample solutions obtained were loaded on Biorad chromatographic columns filled with 2 mL of AG1-X8 (100–200 mesh) anion-exchange resin, cleaned and conditioned with alternating passages of 10 mL of Milli-Q (mQ) water, 10 mL of 1 M $HNO_3$, and 10 mL of 6 M HCl. After loading the sample, the sample matrix was stripped by two rinsing steps of 4 mL of 6 M HCl each. Copper was collected first 50 mL of 8 M HCl. Then, Fe was collected using 20 mL of 0.5 M HCl. Finally, Zn was collected using 15 mL of 1 M $HNO_3$. To further purify the Cu cut from the remaining matrix elements, a second step of anion-exchange chromatographic isolation

**Table 1**
Fe, Cu, and Zn isotope data determined by MC-ICP-MS for the 35 IODP-ICDP Exp. 364 and both UNAM 5 and 7 samples.

| Sample ID[1] | Depth (mbsf)[2] | Lithological unit[3] | | $Fe_2O_3$[4] (wt.%) | $\delta^{56/54}Fe_{IRMM-14}$ (‰) | 2SD | Cu (ppm) | $\delta^{65/63}Cu_{NIST\ SRM\ 976}$ (‰) | 2SD | Zn (ppm) | $\delta^{66/64}Zn_{JMC-Lyon}$ (‰) | 2SD |
|---|---|---|---|---|---|---|---|---|---|---|---|---|
| 40_1_28_30 | 616.52 | Paleogene sediments | | 2.87 | −0.95 | 0.08 | 121 | 0.07 | 0.05 | 79 | 0.49 | 0.01 |
| 40_1_38_44 | 616.62 | Transitional unit | | 1.10 | −0.03 | 0.12 | 32 | −0.72 | 0.08 | 64 | 0.36 | 0.02 |
| 40_1_49_50 | 616.73 | | | 1.72 | 0.23 | 0.15 | 48 | −0.45 | 0.10 | 30 | 0.44 | 0.01 |
| 40_1_80_81 | 617.04 | | | 1.07 | 0.09 | 0.05 | 10 | −0.52 | 0.10 | b.d.l.[5] | 0.80 | 0.04 |
| 40_1_106_110 | 617.30 | | | 5.16 | −0.03 | 0.02 | 53 | −0.24 | 0.04 | 116 | 0.43 | 0.04 |
| 40_1_111_113 | 617.35 | Suevite | Bedded suevite | 8.47 | −0.34 | 0.01 | 28 | −0.48 | 0.03 | b.d.l. | 0.40 | 0.02 |
| 40_2_0_3 | 617.67 | | | 2.09 | 0.05 | 0.02 | 25 | −0.27 | 0.08 | 3 | 0.29 | 0.02 |
| 40_2_100_103 | 618.67 | | | 3.80 | −0.11 | 0.05 | 22 | −0.21 | 0.03 | b.d.l. | 0.43 | 0.02 |
| 44_1_46_48 | 628.90 | | Graded suevite | 4.57 | 0.01 | 0.08 | 43 | −0.11 | 0.01 | 2 | 0.33 | 0.05 |
| 48_1_22_24 | 640.86 | | | 5.08 | 0.04 | 0.02 | 46 | −0.37 | 0.02 | 11 | 0.14 | 0.03 |
| 49_3_56_58 | 646.64 | | | 4.90 | 0.09 | 0.10 | 38 | −0.11 | 0.07 | 46 | 0.24 | 0.01 |
| 51_1_12_14 | 649.94 | | | 4.67 | 0.14 | 0.04 | 145 | −0.11 | 0.04 | 13 | 0.37 | 0.04 |
| 54_1_64_66 | 659.58 | | | 4.96 | 0.07 | 0.08 | 45 | 0.04 | 0.01 | 10 | 0.24 | 0.03 |
| 56_1_95_97 | 665.99 | | | 4.43 | 0.07 | 0.02 | 40 | −0.39 | 0.04 | 31 | 0.10 | 0.02 |
| 59_2_74_76 | 675.91 | | | 4.98 | 0.04 | 0.09 | 31 | −0.28 | 0.03 | 45 | 0.02 | 0.02 |
| 60_1_45_47 | 677.69 | | | 4.71 | 0.07 | 0.10 | 24 | −0.12 | 0.02 | 46 | 0.24 | 0.04 |
| 67_1_13_15 | 690.59 | | | 3.11 | 0.08 | 0.10 | 21 | −0.25 | 0.02 | b.d.l. | 0.20 | 0.03 |
| 78_1_76_78 | 704.50 | | | 1.38 | −0.05 | 0.02 | 27 | −0.07 | 0.04 | 45 | 0.23 | 0.05 |
| 83_1_115_119 | 713.23 | | Non-graded suevite | 3.64 | 0.01 | 0.05 | 6 | −0.11 | 0.02 | 38 | 0.31 | 0.01 |
| 87_2_56_58 | 721.28 | Upper impact melt rock | | 3.77 | 0.12 | 0.03 | 10 | −0.55 | 0.01 | 29 | 0.25 | 0.02 |
| 87_2_73_75 | 721.45 | | | 4.41 | −0.02 | 0.08 | 7 | −0.73 | 0.08 | 34 | 0.32 | 0.01 |
| 89_1_57_59 | 726.21 | | | 4.86 | 0.23 | 0.07 | 31 | −0.49 | 0.04 | 68 | 0.39 | 0.03 |
| 91_1_44_46 | 732.18 | | | 6.11 | 0.17 | 0.06 | 15 | −0.08 | 0.04 | 91 | −0.12 | 0.04 |
| 93_1_19_21 | 738.03 | | | 5.22 | 0.18 | 0.03 | 39 | −0.50 | 0.03 | 49 | −0.49 | 0.06 |
| 95_1_52_54 | 744.46 | | | 4.62 | 0.14 | 0.07 | 56 | −0.05 | 0.06 | 71 | 0.34 | 0.08 |
| 112_2_52_54 | 794.49 | Granite | | 1.26 | 0.16 | 0.12 | 13 | −0.40 | 0.07 | 24 | 0.25 | 0.01 |
| 144_1_19_21 | 865.47 | Dolerite | | 14.02 | 0.13 | 0.05 | 106 | −0.15 | 0.06 | 84 | 0.18 | 0.03 |
| 144_3_3_5 | 867.95 | Granite | | 1.25 | 0.18 | 0.09 | 4 | 0.14 | 0.09 | 6 | 0.31 | 0.02 |
| 169_2_97_99 | 934.83 | Dolerite | | 14.49 | 0.15 | 0.05 | 120 | −0.06 | 0.08 | 79 | 0.23 | 0.02 |
| 222_1_11_13 | 1084.69 | Dolerite | | 11.81 | 0.06 | 0.08 | 112 | −0.39 | 0.05 | 64 | 0.17 | 0.01 |
| 264_1_53_55 | 1212.67 | Granite | | 1.93 | 0.12 | 0.12 | 6 | 0.01 | 0.04 | 31 | 0.31 | 0.09 |
| 276_3_93_95 | 1252.33 | Metamorphic clast (Gneiss) | | 10.82 | 0.12 | 0.04 | 18 | −0.34 | 0.03 | 34 | 0.87 | 0.03 |
| 283_2_46_48 | 1272.97 | Lower impact melt rock | | 6.96 | −0.02 | 0.05 | 87 | −0.19 | 0.03 | 76 | 0.32 | 0.08 |
| 288_1_75.5_77.5 | 1287.30 | Granite | | 1.76 | 0.18 | 0.04 | 10 | −0.63 | 0.01 | 26 | 0.26 | 0.02 |
| 293_1_49_52 | 1301.08 | Lower impact melt rock | | 5.68 | 0.03 | 0.05 | 73 | −0.42 | 0.04 | 64 | 0.34 | 0.02 |
| U5_500.55_500.65 | | Impact breccia | | 2.82 | 0.58 | 0.15 | 40 | −0.01 | 0.05 | 46 | 0.19 | 0.06 |
| U7_267.40_267.50 | | | | 1.80 | 0.06 | 0.08 | 2 | 0.02 | 0.01 | 18 | 0.15 | 0.04 |

*Notes:* Concentration data for Hole M0077A drill core samples are from de Graaff et al. (2022) and Kaskes et al. (2022). [1] Sample nomenclature: Core#_Section#_Top(cm)_Bottom(cm); [2] mbsf = meter below sea floor; [3] subdivision of lithological units and suevite subunits defined by Kaskes et al. (2022); [4] $Fe_2O_3$ anhydrously normalized; [5] b.d.l. = below detection limit.

utilizing a Biorad miniature column was performed. These mini-columns were filled with 0.5 mL of AG1-X8 (200–400 mesh) resin, prepared and conditioned with alternating passages of 10 mL of mQ water, 10 mL of 8 M HCl, and 10 mL of 1 M $HNO_3$. The Cu fraction collected from the first column was evaporated to dryness and taken up in 1 mL of 8 M HCl, and 20 μL of $H_2O_2$ were added just before loading the sample solution onto the columns. After loading this Cu-containing solution on the column, two rinsing steps with 1 mL of 8 M HCl each were used to wash off the matrix, followed by collection of the purified Cu with 10 mL of 8 M HCl.

The Fe isotope ratios were measured at the Atomic & Mass Spectrometry (A&MS) lab of Ghent University (UGent) using a ThermoFisher Scientific Neptune multi-collector inductively coupled plasma-mass spectrometer (MC-ICP-MS) equipped with a large volume interface forevacuum pump and high transmission "jet" interface. The solution was aspirated using a concentric pneumatic nebulizer installed onto a double-volume spray chamber with a cyclonic and a Scott-type subunits, and the isotope ratios were measured interference-free at pseudo-medium mass resolving power (m/Δm ~3800 using 5%–95% notation). The Fe isotopic data presented in this study, are expressed in permil (‰) deviation from the IRMM-014 Fe isotope certified reference material solution using the delta ($\delta$) notation, as indicated in Eq. (1).

$$\delta^{56/54}\mathrm{Fe}_{\mathrm{IRMM-014}} = \left( \frac{\left(^{56}\mathrm{Fe}/^{54}\mathrm{Fe}\right)_{\mathrm{sample}}}{\left(^{56}\mathrm{Fe}/^{54}\mathrm{Fe}\right)_{\mathrm{IRMM-014}}} - 1 \right) \times 1000 \quad (1)$$

The protocol followed here was similar to that published by González de Vega et al. (2020). Mass bias correction was carried out using external correction, with the external standard measured in a sample-standard bracketing sequence and internal correction, via doping the sample solutions with a 500 $ng \cdot g^{-1}$ nickel solution, following the mass bias correction protocol described by Baxter et al. (2006). During data acquisition, repeated measurements of IRMM-014 Fe solution yielded an average value of $\delta^{56/54}$Fe = +0.00 ± 0.07‰ ($n$ = 23), which may be used as an estimate of the intermediate precision. In this study, all reported Fe isotope ratio data represent average values of at least 3 replicate analyses. For consistency, multiple independent digestions of reference material BHVO-2 were measured regularly, and the average $\delta^{56/54}$Fe = 0.11‰ ± 0.06‰ ($n$ = 3) thus obtained is in excellent agreement with literature data (e.g., 0.12‰ ± 0.03‰ in González de Vega et al., 2020 and 0.10‰ ± 0.05‰ in Doucet et al., 2020 and references therein).

The Cu and Zn isotope ratios were determined at the ULB using a Nu Plasma II MC-ICP-MS in operation in either dry or wet plasma modes depending on the Cu and Zn concentrations of the samples. Similar to the Fe isotope measurements, the measurement protocols for Cu and Zn also relied on sample-standard bracketing and doping using Zn and Cu, respectively. The Cu and Zn isotopic data presented in this study are all expressed in permil (‰) using the delta ($\delta$) notation relative to the NIST SRM 976 Cu and the JMC-Lyon Zn isotope reference materials, as indicated in Eqs. (2) and (3), respectively.

$$\delta^{65/63}\mathrm{Cu}_{\mathrm{NIST\ SRM\ 976}} = \left( \frac{\left(^{65}\mathrm{Cu}/^{63}\mathrm{Cu}\right)_{\mathrm{sample}}}{\left(^{65}\mathrm{Cu}/^{63}\mathrm{Cu}\right)_{\mathrm{NIST\ \ SRM\ 976}}} - 1 \right) \times 1000 \quad (2)$$

$$\delta^{66/64}\mathrm{Zn}_{\mathrm{JMC-Lyon}} = \left( \frac{\left(^{66}\mathrm{Zn}/^{64}\mathrm{Zn}\right)_{\mathrm{sample}}}{\left(^{66}\mathrm{Zn}/^{64}\mathrm{Zn}\right)_{\mathrm{JMC-Lyon}}} - 1 \right) \times 1000 \quad (3)$$

The isotope ratios of Cu and Zn were initially measured in sample standard bracketing sequence with in-house Cu and Zn standard solutions, and later the delta notations were converted to values relative to JMC-Lyon and NIST SRM 976 using the known isotopic compositions of the in-house solutions. These in-house solutions of Cu and Zn were respectively calibrated against the NIST SRM 976 Cu and the JMC-Lyon Zn reference standard following Petit et al. (2008). The mass bias correction protocol relied on is described in detail by Doucet et al. (2020). In this study, all the reported Cu and Zn isotope ratio data represent an average value based on at least 3 replicate analyses of the same sample solution. For consistency, fully digested duplicates of reference material BHVO-2 were measured regularly, and the average values obtained, $\delta^{65/63}$Cu = 0.08‰ ± 0.03‰ ($n$ = 3) and $\delta^{66/64}$Zn = 0.30‰ ± 0.03‰ ($n$ = 3), are in good agreement with literature data (Doucet et al., 2020 and references therein). All isotopic uncertainties in this study are expressed with a two standards deviation (2SD).

## 4. Results

### 4.1. Geochemical compositions

The samples selected in this study have been investigated in detail for their petrography and major and trace element geochemistry and found representative for the different target lithologies and impactite intervals. The $SiO_2$, CaO, and MgO concentrations of the selected samples determined by de Graaff et al. (2022) and Kaskes et al. (2022) fall within the range of their respective lithologies (Fig. 2a–c). For these elements, the samples (especially granitoids, metamorphic clast, and LIMB) are in range of the average upper continental crust (UCC) composition determined by Rudnick and Gao (2003). The two UNAM samples exhibit lower $SiO_2$ values, but higher CaO and MgO values than most of the Hole M0077A drill core samples (Fig. 2a–c).

The $Fe_2O_3$ concentrations range from ~1 wt.% to 14.5 wt.% (Fig. 2d), with the granitoids, specific transitional unit and suevite samples, and the U7_267.40_267.50 sample exhibiting the lowest values (~1 wt.% to 2 wt.% $Fe_2O_3$). All UIM and LIMB, most of the suevite samples, and the U5_500.55_500.65 sample display limited variation, ranging between ~3 wt.% and 7 wt.% $Fe_2O_3$, similar to the average UCC value (5.6 wt.% $Fe_2O_3$; Rudnick and Gao, 2003). A single suevite sample (40_1_111_113) displays a value of ~8.5 wt.% $Fe_2O_3$. The highest $Fe_2O_3$ concentrations are found for the dolerite and metamorphic clast samples (~10.8 wt.% to 14.5 wt.% $Fe_2O_3$).

The Cu concentrations range from ~3 to 145 ppm (Fig. 2e), with the granitoids and the U7_267.40_267.50 sample exhibiting the lowest values (~3 to 13 ppm Cu). All UIM, suevite (except 51_1_12_14), and transitional unit samples display a limited variation between ~6 ppm and 56 ppm Cu. The latter range also includes the metamorphic clast (18 ppm Cu), the U5_500.55_500.65 sample (40 ppm Cu), and the average UCC value (28 ppm Cu; Rudnick and Gao, 2003). Higher Cu contents are found for the LIMB and dolerites (~80 and ~112 ppm, respectively). An outlier of the graded suevite subunit (51_1_12_14) and the Paleogene sediments display the highest Cu concentrations within the sample selection with 145 and 121 ppm, respectively.

The Zn concentrations range from ~2 ppm to 116 ppm (Fig. 2f), with one granitoid (144_3_3_5) and several suevite samples from the bedded and graded subunits exhibiting the lowest values (~2 ppm to 13 ppm Zn). Most of the granitoids, the metamorphic clast, and the U7_267.40_267.50 sample range from ~20 ppm to 35 ppm Zn. The U5_500.55_500.65 sample has a Zn concentration of 47 ppm. The Paleogene sediments, dolerites, and lower impact melt rocks exhibit higher values (~64 ppm to 84 ppm Zn), and they are close to the average UCC value of 67 ppm (Rudnick and Gao, 2003). The three lithologies displaying the widest ranges in Zn content are the transitional unit (30 ppm to 116 ppm Zn), the suevite unit (2 ppm to 58 ppm Zn), and the upper impact melt rock (29 ppm to 91 ppm Zn).

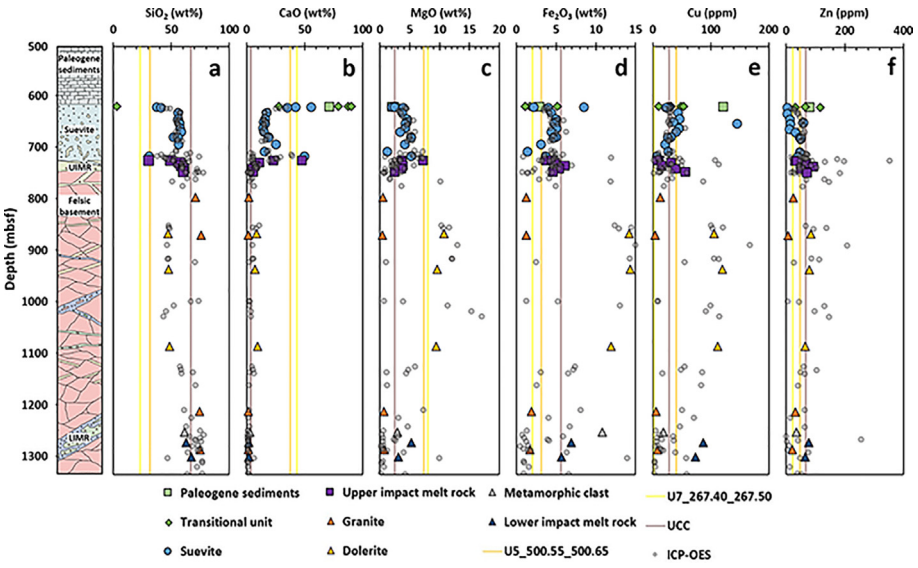


**Fig. 2.** Chemostratigraphic profiles of the $SiO_2$ (a), CaO (b), MgO (c), and $Fe_2O_3$ (d) (in wt.%), and of the Cu (e) and Zn (f) (in ppm) concentrations. UNAM data are from this study. All data for Hole M0077A drill core are from de Graaff et al. (2022) and Kaskes et al. (2022). Average upper continental crust (UCC) values are from Rudnick and Gao (2003). Hole M0077A drill core log is from Morgan et al. (2016). All data are recalculated and normalized on a volatile-free basis, with iron expressed as total ferric iron ($Fe_2O_3^T$).

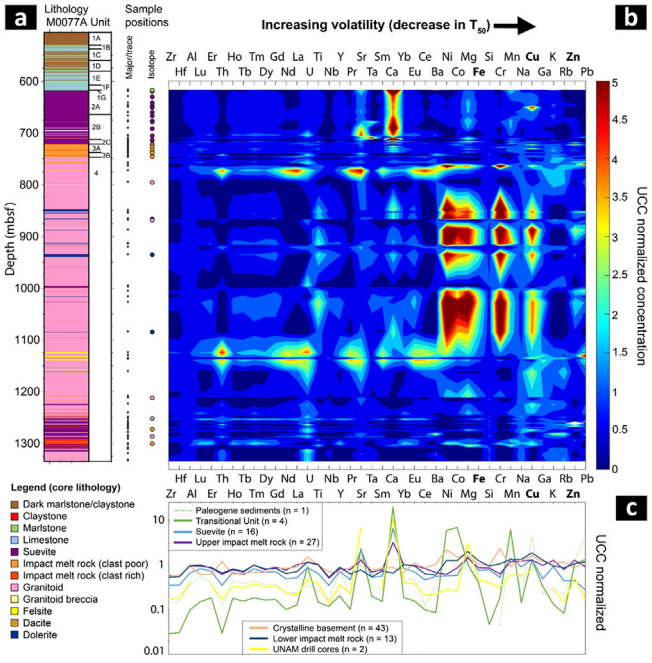


**Fig. 3.** Upper continental crust (UCC) normalized major and trace element concentrations (40) for Hole M0077A drill core samples. (a) Positions of samples analyzed for "major/trace" element contents and for "isotope" ratios along the M0077A drill core log (modified from Kaskes et al., 2022). (b) Stratigraphic contourplot with the UCC normalized values displayed on a color scale. Elements are ordered from more refractory (left) to more volatile (right) based on their 50% condensation temperature ($T_{50}$; Wood et al., 2019). Interpolation was used to fill in the gaps between samples. This allows a general overview of the core but is not meant to be quantitative. (c) Average values for the main lithological units of Hole M0077A drill core (Paleogene sediments, transitional unit, suevite, upper impact melt rock, basement, and lower impact melt rock) and the UNAM samples. UNAM data are from this study. All data for Hole M0077A drill core are from de Graaff et al. (2022) and Kaskes et al. (2022). Average UCC values are from Rudnick and Gao (2003). For an in-depth description and analysis of the individual units see Gulick et al. (2019), Goderis et al. (2021), Feignon et al. (2021, 2022), de Graaff et al. (2022), and Kaskes et al. (2022).

The variation in 40 major and trace element concentrations throughout the entire Hole M0077A drill core shows distinct patterns within some lithological units (Fig. 3b), as also observed in previous studies (Gulick et al., 2019). Normalized to the average UCC values, the upper intervals are enriched in Sr (>~720 mbsf) and in Ca (>~740 mbsf). Nickel, Co, Mg, Fe, Cr, Mn, and Cu are clearly enriched in the interval between ~825 and 1125 mbsf, except where dolerite dikes are occurring. Minor Zn enrichments are observed at ~721, 887, 1027, and 1266 mbsf. No systematic trends for depletion in volatile elements (Mn, Na, Cu, Ga, K, Rb, Zn, Pb) for any particular interval of the drill core can be discerned (Fig. 3b). As the interpolation between samples may in some cases strongly influence the visual appearance of the element distribution, any interpretation must be evaluated carefully. It is important to keep in mind that the Paleogene sediments are only represented by a single sample and the transitional unit is too thin (<1 m) to be correctly represented (Fig. 3b). To counter this effect and allow a comparison with UNAM samples, the average values per lithological units are used (Fig. 3c). This approach confirms high concentrations for Ca and Sr in the Paleogene sediments, the transitional unit, the suevite, and the UNAM samples, and also to a lesser extent in the UIM. A high Mn concentration is observed in the Paleogene sediments and the transitional unit. High Ni and Co concentrations are associated with the transitional unit, which are most probably linked to the settling of meteoritic material within this interval (Goderis et al., 2021; Feignon et al., 2022). A more conventional plot of the rare earth element (REE) concentrations normalized to average values for CI chondrite can be found in Fig. 4.

### 4.2. Fe, Cu and Zn isotopic ratios

The $\delta^{56/54}$Fe results fall within a narrow range between ~−0.1‰ and 0.2‰ (Fig. 5a), in range of the values typically obtained for the UCC (0.09‰ ± 0.03‰, Gong et al., 2017). The sample from the U7 drill core also falls within this range with a $\delta^{56/54}$Fe value of 0.06 ‰ ± 0.08‰. More strongly fractionated values are measured for the Paleogene sediment ($\delta^{56/54}$Fe down to −0.95‰ ± 0.08‰ for 40_1_28_30) and the uppermost sample of the bedded suevite ($\delta^{56/54}$Fe down to −0.34‰ ± 0.01‰ for 40_1_111_113). In contrast, a distinctly higher $\delta^{56/54}$Fe value of 0.58‰ ± 0.15‰ is found for the

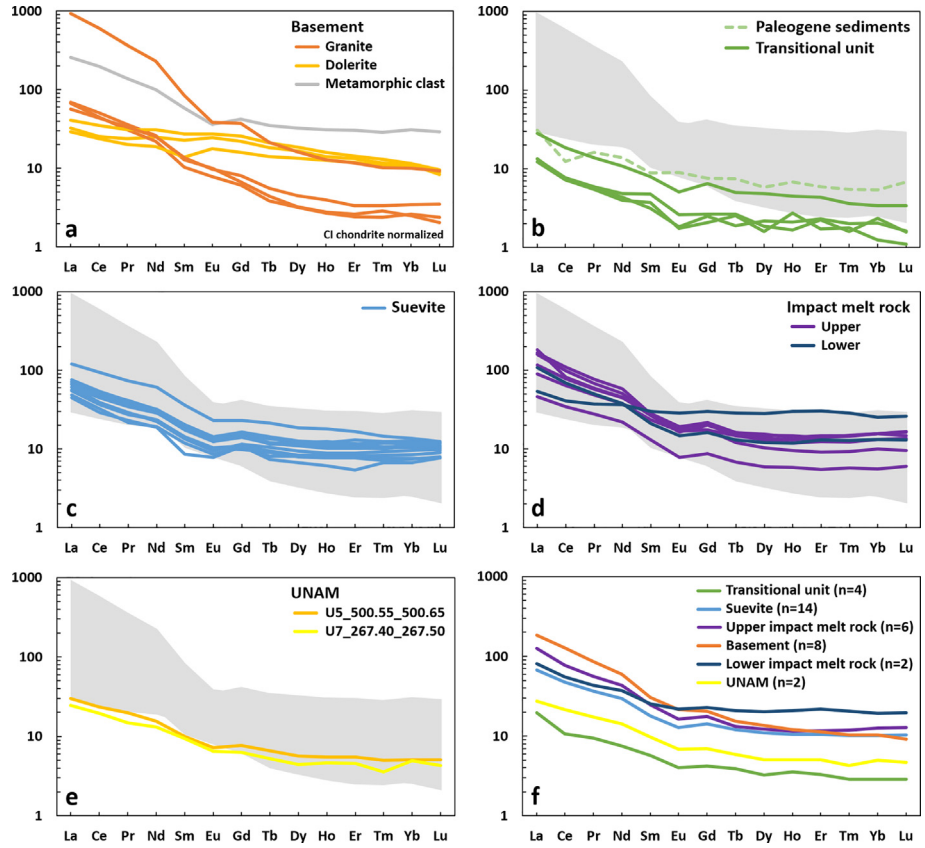


**Fig. 4.** CI chondrite normalized rare earth element (REE) concentrations, with normalization values from McDonough and Sun (1995). Basement samples (a) are represented by the grey envelope with the Paleogene sediments and transitional unit samples (b); the suevites (c); the upper and lower impact melt rocks (d); and the UNAM samples (e). Average values for each lithology (f). UNAM data are from this study. All data for Hole M0077A drill core are from de Graaff et al. (2022) and Kaskes et al. (2022).

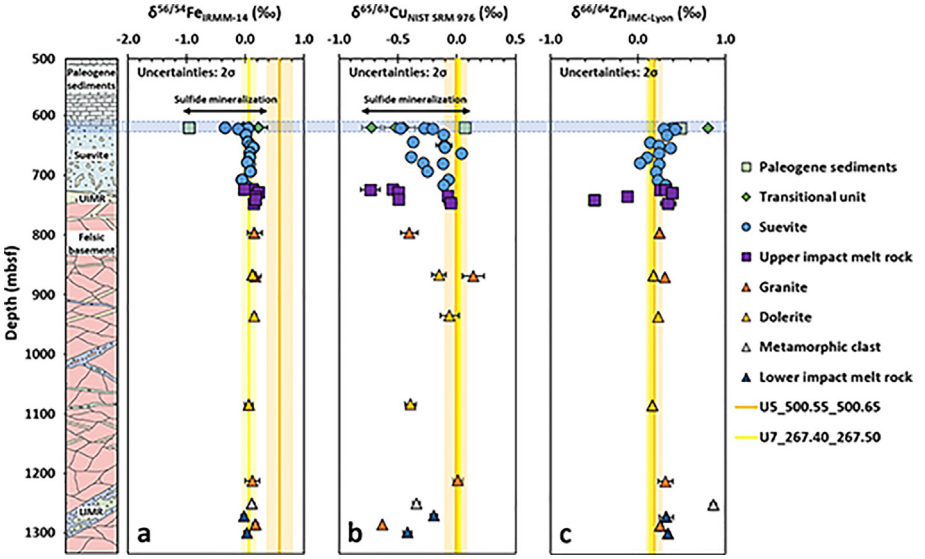


**Fig. 5.** Chemostratigraphic plots for the $\delta^{56/54}$Fe (a), $\delta^{65/63}$Cu (b), and $\delta^{66/64}$Zn (c) values. Hole M0077A drill core log is from Morgan et al. (2016). Error bars reflect two times the standard deviation. Where error bars are not visible, uncertainties are smaller than the symbol size. Data are shown in Table 1. Blue envelope shows the area plotted in Fig. 7.

sample U5_500.55_500.65. The largest Fe isotope variability is observed for the suevite unit ranging from −0.34‰ to 0.14‰ (Fig. 5a; Table 1). The $\delta^{56/54}$Fe of the UIM unit (0.14‰ ± 0.02‰, $n$ = 7) overlaps with that of the target rocks (0.14‰ ± 0.01‰, $n$ = 8; Table 2). However, the average $\delta^{56/54}$Fe values of the suevite (0.02‰ ± 0.01‰, $n$ = 17) and LIMB (0.00 ± 0.04‰, $n$ = 2) units fall slightly below those of the averaged target rocks (Table 2).

The $\delta^{65/63}$Cu results display a wide variability ranging from ~−0.73‰ to 0.14‰ in all measured impactites and target rocks (Fig. 5b). Contrary to the Fe isotope ratio data, the Cu isotope ratio

**Table 2**
Average Fe, Cu, and Zn isotope compositions of the different lithologies within the M0077A and UNAM 5 and 7 drill cores.

| Drill core | Lithological unit | *n* | $\delta^{56/54}Fe_{IRMM-14}$ (‰) | 2SD (‰) | $\delta^{65/63}Cu_{NIST\ SRM\ 976}$ (‰) | 2SD (‰) | $\delta^{66/64}Zn_{JMC-Lyon}$ (‰) | 2SD (‰) |
|---|---|---|---|---|---|---|---|---|
| Hole M0077A | Paleogene sediments | 1 | −0.95 | 0.08 | 0.07 | 0.05 | 0.49 | 0.01 |
| | Transitional unit | 4 | −0.14 | 0.19 | −0.48 | 0.10 | 0.51 | 0.10 |
| | Suevite | 17 | 0.02 | 0.01 | −0.25 | 0.02 | 0.24 | 0.01 |
| | Upper impact melt rock | 7 | 0.14 | 0.02 | −0.41 | 0.07 | 0.01 | 0.12 |
| | Target rocks | 8 | 0.14 | 0.01 | −0.23 | 0.06 | 0.32 | 0.06 |
| | Lower impact melt rock | 2 | 0.00 | 0.04 | −0.31 | 0.16 | 0.33 | 0.01 |
| | Upper impact melt rock without negative outliers | 5 | | | | | 0.33 | 0.03 |
| | Target rocks without metamorphic clast (gneiss) | 7 | | | | | 0.24 | 0.02 |
| U5 & U7 | Impact breccia | 2 | 0.32 | 0.37 | 0.01 | 0.02 | 0.17 | 0.03 |

*Notes:* total number of samples for Hole M0077A drill core is above 35 as some samples were duplicated.

data for individual units exhibit a similar range in values. The average values per unit indicate that the Cu isotopic compositions are comparable for the suevite and the target rock units, with $\delta^{65/63}$Cu values of −0.25‰ ± 0.02‰ ($n$ = 17) and −0.23‰ ± 0.06‰ ($n$ = 8; Table 2). On the other hand, the UIM and LIMB units display lower average $\delta^{65/63}$Cu values of −0.41‰ ± 0.07‰ ($n$ = 7) and −0.31‰ ± 0.16‰ ($n$ = 2), respectively. Considerable variation also exists within the UIM unit, which appears to depend on the presence or absence of dark green schlieren. The three UIM samples containing green schlieren plot towards lower $\delta^{65}/^{63}$Cu values, especially in the case of sample 87_2_73_75, which is entirely composed of green schlieren and exhibits the lowest value of all impact melt rocks ($\delta^{65/63}$Cu of −0.73‰ ± 0.08‰; Fig. 5b, Table 1). The Paleogene sediment displays a $\delta^{65/63}$Cu value of 0.07‰ ± 0.05 ‰, comparable to those measured for both UNAM samples (−0.01‰ ± 0.05‰ and 0.02‰ ± 0.01‰ for samples U5_500.55_500.65 and U7_267.40_267.50, respectively).

The $\delta^{66/64}$Zn results also exhibit a wide range of values from ~−0.49‰ to 0.87‰. However, this large magnitude does not affect all lithologies. Most samples from the Hole M0077A drill core display limited variation, with most values varying between ~0.0 and 0.4‰, fully in the range of the UCC values (Pons et al., 2013; Fig. 4c). Both UNAM samples also fall within this range with a $\delta^{66/64}$Zn value of 0.19‰ ± 0.06‰ for the sample U5_500.55_500.65 and of 0.15‰ ± 0.04‰ for the sample U7_267.40_267.50 (Table 1). Two black upper impact melt rock samples (91_1_44_46 and 93_1_19_21) have distinctly lower $\delta^{66/64}$Zn values of −0.12‰ ± 0.04‰ and −0.49‰ ± 0.06‰, respectively. In contrast, the metamorphic clast (276_3_93_95) and one sample from the transitional unit (40_1_80_81) show higher $\delta^{66/64}$Zn values of 0.87‰ ± 0.03‰ and 0.80‰ ± 0.04‰, respectively. After exclusion of the two low-value outliers, the UIM and LIMB units have $\delta^{66/64}$Zn values identical to those of the target rocks within the 2SD uncertainty (Table 2). On average, the suevite unit is isotopically lighter ($\delta^{66/64}$Zn = 0.24‰ ± 0.01‰, $n$ = 17), while the transitional unit ($\delta^{66/64}$Zn = 0.51‰ ± 0.10‰, $n$ = 4) is isotopically heavier than the other lithological units. In addition, the suevite unit has an average $\delta^{66/64}$Zn value identical to that of the target rock without the metamorphic clast sample (Table 2).

## 5. Discussion

As shown above, even by taking into account the volatility of elements, no systematic trends are observed for the major and trace elemental compositions within the Hole M0077A lithologies (Fig. 3). This combined with the observation that the lithological units and subunits (e.g., within the suevite) were likely subjected to distinct thermodynamic conditions during their deposition implies that isotopic systems need to be applied to disentangle the processes occurring during and after the impact. This may be feasible because the selected bulk samples are petrographically and geochemically representative of their respective lithological units (Figs. 2 and 3). Hence, the variations observed are in large part due to thermodynamic processes and not linked to sample heterogeneities. While the observed isotopic deviations may not represent the most extreme ranges due to homogenization of the bulk sample powders, obliterating any isotopic variability at the microscale, the distinct geochemical properties and behavior of Fe, Cu, and Zn are exploited here to untangle a range of processes taking place during impact cratering events.

### 5.1. Late-stage hydrothermal overprinting, secondary alteration, and diagenesis

An impact-induced hydrothermal system affected the entire Chicxulub impact structure for at least a couple of millions of years after impact (Kring et al., 2020). Before the isotopic and geochemical signatures measured here can be interpreted, the effects of secondary processes on the various units need to be carefully evaluated. Replacement of mineral phases can lead to mineral-driven isotopic fractionation under low-temperature equilibrium conditions at the bulk rock scale. Pervasive alteration of the Chicxulub impact structure lithologies is apparent in the form of widespread replacement of vitric melt particles by phyllosilicates, chloritization and serpentinization of mafic minerals, subsequent conversion of chlorite to phyllosilicates, and extensive calcite crystallization in veins (e.g., Hecht et al., 2004; Zürcher and Kring, 2004; Tuchscherer et al., 2006; Kring et al., 2020; Simpson et al., 2020; de Graaff et al., 2022), likely as the result of a long-lived (couple of Myr) percolation of hydrothermal fluids (Abramov and Kring, 2007; Kring et al., 2020; Osinski et al., 2020).

Within the impact crater, the main hydrothermal flow occurred nearby the melt pool, close to the peak ring and reached at least 700 mbsf (Kring et al., 2020). Post-impact hydrothermal alteration has also been observed between the peak ring and the crater rim, especially in the Yaxcopoil-1 drill core where it appears as a ~100 m thick hydrothermally altered unit (e.g., Hecht et al., 2004; Zürcher and Kring, 2004). The further away from the crater center, the weaker the hydrothermal overprint of both the target rocks and the impactites. Therefore, the hydrothermal effect should be minimal in the UNAM samples compared to those from the Hole M0077A drill core.

The alteration observed is often accompanied by remobilization of fluid-mobile elements, such as K (Hecht et al., 2004) but also La and Sr (de Graaff et al., 2022). This is also highlighted by the presence of precipitated sulfides crystals and apatite grains within chlorite veins in the transitional unit (Bralower et al., 2020), while the top of the transitional unit is also characterized by the presence of diagenetic pyrite crystals and nodules (Goderis et al., 2021). Hydrothermal channels containing Na-dachiardite, heulandite, analcime, and secondary Fe-Mg clay minerals and calcite have been observed throughout the suevite unit (Kring et al., 2020; Simpson et al., 2020). Cavities are found within the suevite unit, as well as both UIM and LIMB units, which are filled with a wide

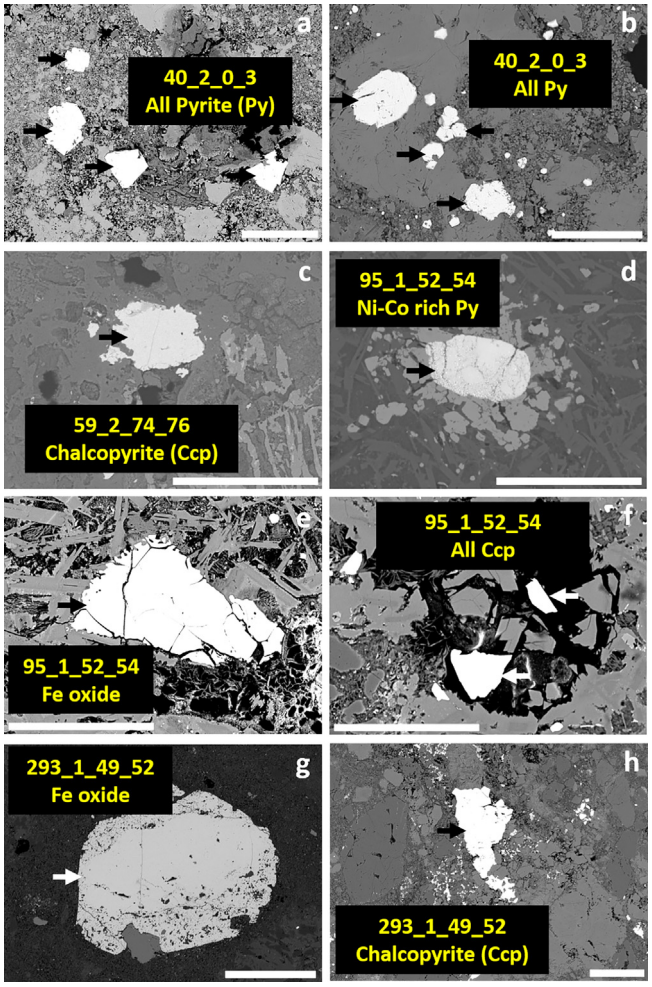


**Fig. 6.** Backscattered electron (BSE) images of sulfides and oxides, indicated by arrows, from different intervals within the Hole M0077A drill core. (a, b) Pyrites from the bedded suevite sample 40_2_0_3. (c) Chalcopyrite from the graded suevite sample 59_2_74_76. (d) Ni-Co rich pyrites, (e) iron (+Mg, Al) oxide, (f) chalcopyrite from the upper impact melt rock sample 95_1_52_54. (g) Iron oxide and (h) chalcopyrite from the lower impact melt rock sample 293_1_49_52. Scale bars represent 100 μm.

variety of secondary minerals such as epidote, barite, sulfides, and the minerals also present in hydrothermal channels mentioned above (Kring et al., 2020). Dissolution features (e.g., quartz dissolution), secondary calcite precipitation, epidote and chlorite veins have been found within the UIM unit and the basement lithologies (Kring et al., 2020; de Graaff et al., 2022). Hydrothermal garnet precipitated within the LIMB unit and the surrounding granitoids at the bottom of the Hole M0077A drill core (Kring et al., 2020). In addition, the conversion to secondary alteration such as phyllosilicates also heavily affected the bulk geochemical composition. The entire Hole M0077A drill core exhibits evidence of an important post-impact hydrothermal overprinting associated to secondary alteration and mineral precipitation. Especially important in this context is the presence of sulfide minerals, as these represent major host phases for Fe, Cu, and Zn.

### *5.2. Mineralogy driving observed isotopic variation in Expedition 364 core*

Several types of sulfide and iron oxide minerals are observed in the thin sections and have been characterized by SEM-EDS. Occurring in all lithologies, especially the transitional unit, suevite, UIM, and LIMB, they consist mostly of pyrites occasionally enriched in Ni and Co, iron oxides occasionally enriched in Mg and Al, and chalcopyrites (Fig. 6). No Zn sulfides such as sphalerite have been found within the analyzed samples.

Pyrites ($FeS_2$) have been found almost throughout the entire Hole M0077A drill core, within basal Paleogene sediments, transitional unit, suevite, UIM, LIMB, and many granitoid samples (Bralower et al., 2020; Kring et al., 2020; de Graaff et al., 2022). The transitional and suevite units exhibit sulfide mineralizations associated to vertical venting channels (Kring et al., 2020). Framboidal pyrites ($FeS_2$) have been identified in the upper part of the core, above 700 mbsf (Kring et al., 2020, Goderis et al., 2021). Chalcopyrites ($CuFeS_2$) are present mostly within the suevite unit, the UIM, and the LIMB (Kring et al., 2020; Goderis et al., 2021). Sphalerite (ZnFeS) has so far only been found in the green marlstone (basal Paleogene sediments) and in the uppermost part of bedded suevite (Bralower et al., 2020; Goderis et al., 2021). Epidote and clay minerals (such as chlorite, saponite, serpentinite, and smectite) can also host Fe within the core, and they are present within the entire basement material and the whole Hole M0077A drill core, respectively (Kring et al., 2020; de Graaff et al., 2022). These main host phases are secondary minerals formed at elevated temperature (>250–300 °C) and have been linked to fluid alteration processes during the cooling of the Chicxulub hydrothermal system (Kring et al., 2020). As no other specific mineralogical host phases have been identified in previous studies, nor in this one, the different secondary host phases of Fe described above precipitated from fluids circulating throughout the entire impact structure and affecting all lithological units. This likely explains most of the homogenized Fe isotopic compositions (Fig. 5). Hence, the primary bulk rock Fe isotopic signatures of the distinct lithological units have likely been overprinted to a large extent.

Light Fe isotope ratio values are preserved within the top part of the Hole M0077A drill core (Fig. 7a). The two samples carrying light Fe isotopic signatures are the Paleogene sediments (40_1_28_30) with a $\delta^{56/54}$Fe value of −0.95‰ ± 0.08‰ and the uppermost sample of the suevite unit (sample 40_1_111_113, 2 cm below the sharp contact between transitional unit and suevite) with a $\delta^{56/54}$Fe value of −0.34‰ ± 0.01‰. These samples contain sulfides that can be traced by the Fe and S contents of the bulk rock fragments (Fig. 7b–c). In sample 40_1_28_30, these sulfides have been described as two thin concentrated layers associated with cm-sized nodules (Goderis et al., 2021). This specific pyritic interval displays a distinct Fe isotopic signature from all other samples analyzed in this study. As observed at anoxic marine K/Pg sites (e.g., Schmitz et al., 1988; Smit, 1999), the formation of the pyritic interval in sample 40_1_28_30 is likely linked to early anaerobic microbial diagenesis at lower temperature rather than at the formation of the first generation of sulfides from hydrothermal fluids (Goderis et al., 2021). This interpretation is based on the enrichment of these pyrites in specific chalcophile elements (such as As and Sb) and is consistent with the difficulty to precipitate sulfides with such low $\delta^{56/54}$Fe values in equilibrium with seawater (Craddock and Dauphas, 2011). These light Fe isotopic compositions correspond to microbially reduced pyrite formed in normal marine conditions, as such pyrite is known to exhibit fractionated values with respect to the host sediment (Craddock and Dauphas, 2011).

Of the three isotopic systems for which data are reported here, Cu displays the largest variability within the respective lithological units (Fig. 5). Studies of Cu isotopic composition of chalcopyrite mineralization within black smoker chimneys in hydrothermal systems along the mid-oceanic ridges provide a wide range of $\delta^{65/63}$Cu values from ~ −0.9‰ to 3‰ (Zhu et al., 2000; Rouxel et al., 2004). Most negative $\delta^{65/63}$Cu values are found within old inactive vents, while most positive values are displayed by active

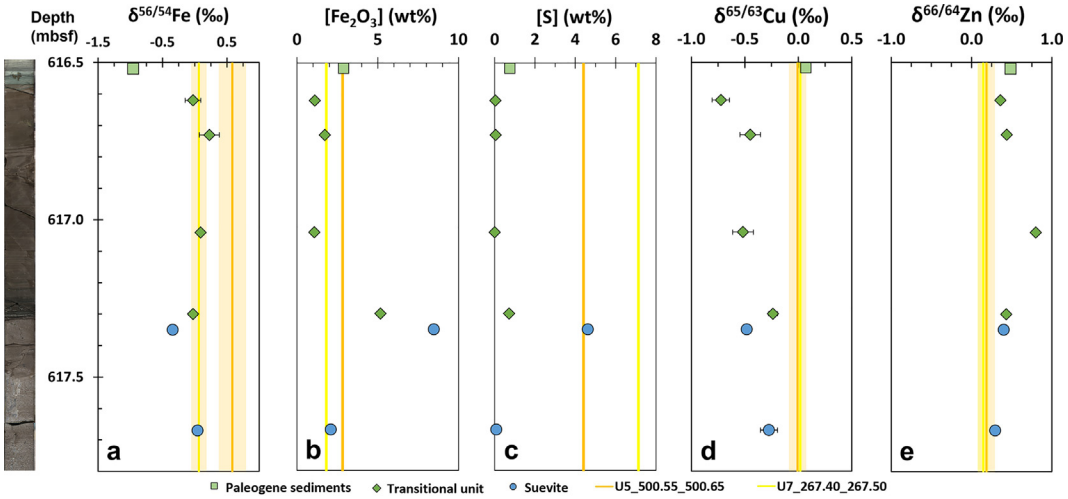


**Fig. 7.** Chemostratigraphic plots for $\delta^{56/54}$Fe (a), $Fe_2O_3$ (b) and S (c) anhydrously normalized concentrations, $\delta^{65/63}$Cu (d), and $\delta^{66/64}$Zn (e) for the top part of the Hole M0077A drill core (basal Paleogene sediments, transitional unit, and bedded suevite). Isotopic data are from this study. Fe and S compositions are from de Graaff et al. (2022) and Kaskes et al. (2022). Error bars reflect two times the standard deviation. Where error bars are not visible, uncertainties are smaller than the datapoint.

hydrothermal vents (Rouxel et al., 2004). Chalcopyrites would first precipitate from the hydrothermal fluids during the cooling of the impact structure with positive $\delta^{65/63}$Cu values (up to ~3‰; Rouxel et al., 2004). Alteration of this first generation of chalcopyrites by seawater could then have led to reprecipitation with lower $\delta^{65/63}$Cu values (down to ~−1‰; Rouxel et al., 2004). As sites outside of the impact structure would be less influenced by such a phenomenon, it can be assumed that the starting $\delta^{65/63}$Cu values have been recorded by the UNAM samples (−0.01‰ ± 0.05‰ for U5_500.55_500.65 and 0.02‰ ± 0.01‰ for U7_267.40_267.50; Fig. 5b and Table 1) and then seawater alteration led to lower $\delta^{65/63}$Cu values (down to −0.73‰ ± 0.08‰ for 87_2_73_75; Fig. 5b and Table 1) within the Chicxulub impact structure. Therefore, all lithologies have been affected by the post-impact hydrothermal activity and the Cu isotopic variability observed is best explained by the heterogeneous distribution of Cu-rich sulfides.

In contrast to Cu, the Zn isotopic profile measured for the Hole M0077A drill core displays only limited variations. Importantly, the occurrence of pyrite in chlorite veins and ZnS within the transitional unit indicate that thin fingers of higher temperature fluids penetrated the buried sediment column and that local hydrothermal activity persisted possibly for a long time after normal hemipelagic deposition resumed (Bralower et al., 2020). Yet, most sampled core intervals from this unit display no deviations from the initial signature (Fig. 5c). Four samples exhibit a Zn isotopic signature that deviates from this initial signature: positive deviations for transitional unit sample 40_1_80_81 (0.80‰ ± 0.04‰) and metamorphic clast sample 276_3_93_95 (0.87‰ ± 0.03‰), and negative deviations for two black UIM samples (−0.12‰ ± 0.04‰ for 91_1_44_46 and −0.49‰ ± 0.06‰ for 93_1_19_21). This indicates that the isotopic signatures of those four samples may not (entirely) be linked to sulfide secondary mineralization.

### 5.3. Isotopic perspective on mixing and melting

The different target lithologies analyzed in this study (granitoid, dolerite, metamorphic rock) display distinct differences in major and trace element compositions (Figs. 2 and 3), yet similar albeit smaller variations for their respective Fe, Cu, and Zn isotopic compositions (Fig. 5). The $\delta^{56/54}$Fe values of the three basement lithologies analyzed fall within a narrow range of values (Fig. 5a), leading to a well-defined average $\delta^{56/54}$Fe value of 0.14‰ ± 0.01‰ ($n$ = 8; Table 2). As mentioned above, the $\delta^{65/63}$Cu values of the different target lithologies are scattered over a wide range of values (Fig. 5b and Table 1), which may be linked to secondary effects. Nonetheless, the values for each basement lithology cover this range, which corresponds to an average $\delta^{65/63}$Cu value of −0.23‰ ± 0.06‰ ($n$ = 8; Table 2). The $\delta^{66/64}$Zn values of dolerite and granitoid fall within a narrow range, with dolerite exhibiting slightly lower values than granitoid (Fig. 5c and Table 1). Only the measured metamorphic clast displays an over 0.5‰ higher $\delta^{66/64}$Zn value compared to any other basement sample. The $\delta^{66/64}$Zn value for the average target is 0.32‰ ± 0.06‰ ($n$ = 8; Table 2).

The UIM, LIMB, and suevite unit exhibit major and trace element compositions within the ranges defined by the target lithologies (Figs. 2 and 3). This is interpreted to result from the mixing of felsic granitoids and mafic dolerites (de Graaff et al., 2022). The only exception is the CaO content of the upper impact melt rock and the suevite units, which may be linked to contributions from the carbonate platform to the UIM (de Graaff et al., 2022). The Fe isotopic composition of the LIMB rock (average $\delta^{56/54}$Fe value of 0.00 ± 0.04‰, $n$ = 2) and the suevite ($\delta^{56/54}$Fe = 0.02‰ ± 0.01‰, $n$ = 17,) appear isotopically lighter than the basement ($\delta^{56/54}$Fe = 0.14‰ ± 0.01‰) (Fig. 5a and Table 2). This contrasts with the UIM rock ($\delta^{56/54}$Fe = 0.14‰ ± 0.02‰, $n$ = 7) that fall in the range of the average $\delta^{56/54}$Fe values of the target (Fig. 5a and Table 2). Due to a higher uncertainty, U7_267.40_267.50 overlaps both ranges ($\delta^{56/54}$Fe = 0.06‰ ± 0.08‰), while U5_500.55_500.65 displays a heavier value than any other sample ($\delta^{56/54}$Fe = 0.58‰ ± 0.15‰). The low average $\delta^{56/54}$Fe value of the suevite unit is largely controlled by a few samples with negative isotopic values due to specific sulfide intervals, especially within the bedded suevite subunit (see Section 5.2).

In the case of the Cu isotopic system, the suevite unit displays $\delta^{65/63}$Cu values similar to those of the target rocks (average of −0.25‰ ± 0.02‰, $n$ = 17 versus −0.23‰ ± 0.06‰, $n$ = 8; Table 2). Both the upper and lower impact melt rocks and the transitional unit exhibit lighter average isotopic signatures ($\delta^{65/63}$Cu values of −0.41‰ ± 0.07‰ ($n$ = 7), −0.31‰ ± 0.16‰ ($n$ = 2), and −0.48‰ ± 0.10‰ ($n$ = 4), respectively; Table 2), which are interpreted here to reflect an overprint of the hydrothermal system in the presence of seawater (see Section 5.2). This interpretation is also supported by the UNAM samples, displaying an average $\delta^{65/63}$Cu value of 0.01‰ ± 0.02‰ ($n$ = 2), which is supposed to be the initial Cu iso-

topic value before the occurrence of any hydrothermal overprinting within the Chicxulub impact structure. However, there is substantial variation in $\delta^{65/63}$Cu within each unit, which may be linked to a heterogeneous distribution of specific host phases of Cu. Given the observed scatter, it is difficult to decipher whether mixing and melting homogenized the primary isotopic signatures of the various lithological units.

The lower impact melt rock-bearing unit displays $\delta^{66/64}$Zn values fully in range with the target lithologies (average of 0.33‰ ± 0.01‰, $n$ = 2 versus 0.32‰ ± 0.06‰, $n$ = 8; Table 2). If all samples of the upper impact melt unit are considered, the average $\delta^{66/64}$Zn value of the unit is significantly lower than that of the basement (0.01‰ ± 0.12‰, $n$ = 7; Table 2). However, if the two lowest values are disregarded, the $\delta^{66/64}$Zn value obtained is 0.33‰ ± 0.03‰ ($n$ = 5; Table 2), which falls within error of the target rocks (including the gneiss clast) and lower impact melt rock values. The only lithologies that display heavy Zn isotopic signatures are the Paleogene sediments and the transitional unit (especially sample 40_1_80_81). The value of 40_1_80_81 is comparable to that observed for the gneiss clast 276_3_93_95. As no mineral drivers are observed to explain these positive values, a different process may need to be invoked to explain these Zn isotopic variations (Fig. 5c).

### 5.4. Potential traces of impact volatilization

Recently, Mathur et al. (2021) reported that the Zn isotopic compositions of the K-Pg sedimentary layers closely adhere to a Rayleigh distillation curve, whereby $\delta^{66/64}$Zn increases as Zn concentration decreases. This observation was interpreted to reflect that partial Zn evaporation from impact-generated melt spherules was the process controlling the Zn isotopic and concentration signatures of K-Pg boundary spherules and ejecta layers. Similar to Zn, the near absence of sulfur-rich minerals (<1%) in the Hole M0077A core, which is in stark contrast to the 30% to 50% evaporites in the Yucatán sedimentary target rocks, has been interpreted to reflect impact degassing (Gulick et al., 2019). Paleogene sediments sample 40_1_28_30 together with two samples from the transitional unit (40_1_106_110 and 40_1_80_81; the latter is not plotted in Fig. 8 as the Zn content is below the detection limit but shows a $\delta^{66/64}$Zn value of 0.80‰ ± 0.04‰; Table 1) from the IODP-CDP Exp. 364 core follow the evaporation trends observed for the K-Pg boundary layer sediments around the world and tektites from various strewn fields (Fig. 8). This trend may suggest that the Zn isotope ratios for the upper sections of the drill core may have retained a hint of volatility-driven isotopic fractionation. While one should keep in mind that seawater nodules, tracing seawater Zn isotope ratios, can also display higher $\delta^{66/64}$Zn values (Maréchal et al., 2000), the trends for K-Pg boundary sediments highlighted by Mathur et al. (2021) are observed for both marine and terrestrial sites, confirming the robustness of Zn isotope systematics. In addition, no Zn carrier phases were identified in the Paleogene sediments and transitional unit samples studied here. Intriguingly, the gneiss clast also follows the volatilization trends, albeit representing only a single sample at a specific fractionation factor α. Again, no petrographic or geochemical observations can be linked to this isotopic composition, suggesting this clast may have been subjected to higher degrees of shock and volatilization.

To verify whether the volatilization is a process that can be identified from the data, a Rayleigh distillation model was applied to the Cu and Zn concentrations and isotopic data (Fig. 8). The average Cu and Zn isotopic signatures of the two UNAM samples ($\delta^{65/63}$Cu ~0.0‰ and $\delta^{66/64}$Zn ~0.17‰, respectively) were used as initial parameters, due to the limited hydrothermal alteration that

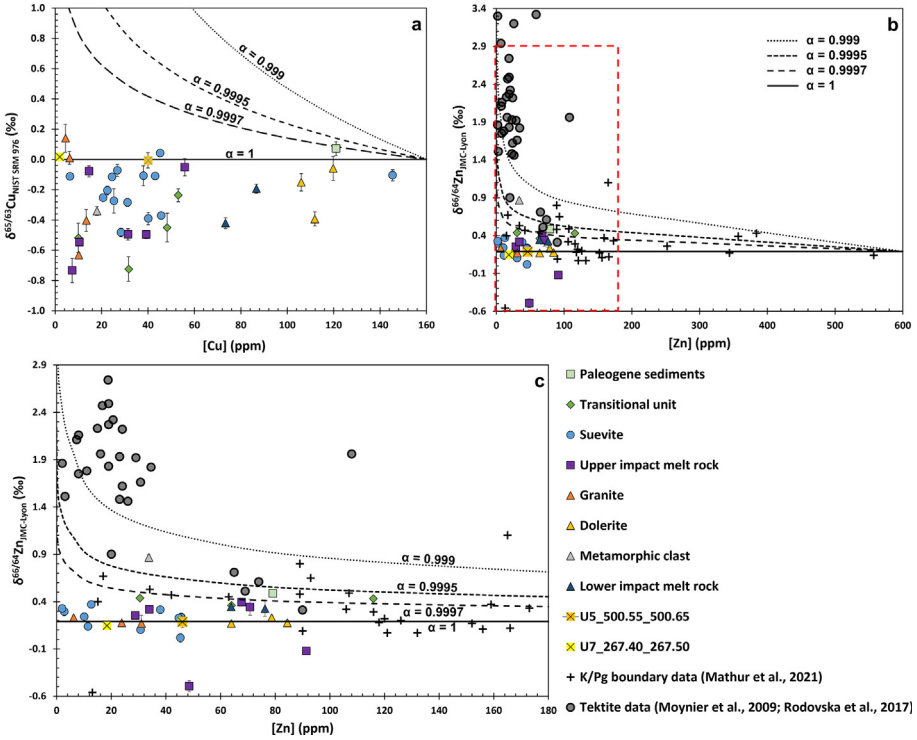


**Fig. 8.** (a) $\delta^{65/63}$Cu versus Cu concentration for the Hole M0077A and UNAM 5 and 7 drill core samples. (b) $\delta^{66/64}$Zn versus Zn concentration for the Hole M0077A and UNAM 5 and 7 drill core samples. (c) Close-up of the Zn graph focusing on the low Zn concentrations (<180 ppm). Curves based on the Rayleigh distillation model are shown for different fractionation factors α (1, 0.9997, 0.9995, 0.999). Cu and Zn concentrations are from de Graaff et al. (2022) and Kaskes et al. (2022). K/Pg boundary data are from Mathur et al. (2021) and tektite data are from Moynier et al. (2009) and Rodovská et al. (2017). Error bars reflect two times the standard deviation. Where error bars are not visible, uncertainties are smaller than the symbol size. Data are shown in Table 1.

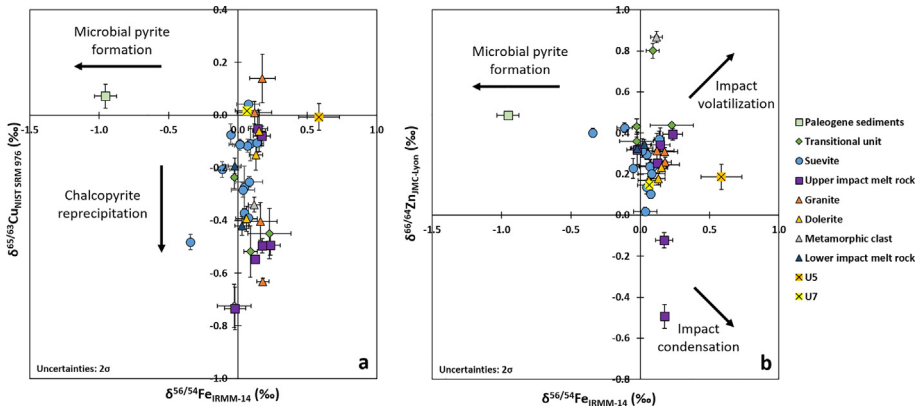


**Fig. 9.** Plots of $\delta^{56/54}$Fe versus $\delta^{65/63}$Cu (a), $\delta^{56/54}$Fe versus $\delta^{66/64}$Zn (b) for the M0077A and UNAM 5 & 7 samples. Arrows indicate the influence of specific processes on the isotopic values. Data are shown in Table 1.

they experienced relative to the Hole M0077A drill core samples (see Sections 5.1 and 5.2). In the case of Cu, none of the 35 Expedition 364 samples fit the Rayleigh distillation model, not even when using a kinetic fractionation factor $\alpha \geq 0.9997$ (Fig. 8a). This implies that any previously recorded volatilization process, which has been observed to exist for Cu based on experimental work (Ni et al., 2021), is no longer preserved in the case of the Cu isotopic system (Fig. 9). Similar results are obtained for Fe. However, several Zn isotope ratio data do fit the curves modelled based on Rayleigh distillation (Fig. 8b-c). The compiled data for the individual isotope systems are compared in Fig. 9.

The empirical factor $\alpha$ for tektite data (0.999 to 0.9997) based on the Zn isotope ratio data determined for distal K-Pg boundary sites (Mathur et al., 2021), and the data collected in this work imply Zn isotopic fractionation from volatilization below that expected by theoretical Rayleigh distillation to vacuum ($\alpha \approx 0.985$ in a vacuum). In all cases, the lower $\alpha$ is likely attributable to effects linked to diffusion in the thin layer of the ejecta, slowing down the evaporation (Moynier et al., 2009; Creech and Moynier, 2019) and/or suppression of Zn isotopic fractionation during large-scale evaporation under high pressure (i.e., non-vacuum) conditions (Davis and Richter, 2014; Day et al., 2017; Wimpenny et al., 2019; Chernonozhkin et al., 2021). While the $\alpha$ envelope of the distal K-Pg ejecta (between roughly 0.999 and 1; Mathur et al., 2021) is well below that of tektites (down to <0.999; Moynier et al., 2009; Rodovská et al., 2017), the Zn data for the core samples plot within an even narrower $\alpha$ range between 0.9995 and 1 (Fig. 8b-c). This change in $\alpha$ has previously been explained by signal dilution due to ejecta mixing with local materials in the K-Pg sedimentary layers (dilution by ~10:1 in the case of ~10% Zn from ejecta) and addition of Zn from non-volatilized sources during sedimentation and lithification (Mathur et al., 2021). In the case of the Hole M0077A drill core samples, a further dilution due to a hydrothermal overprint and homogenization during sample powdering may be envisioned.

### 5.5. Condensation in the upper impact melt rock and link with impact ejecta

Impact ejecta (mainly microtektites) enriched in isotopically heavy Zn require the existence of a reservoir of isotopically lighter Zn within or outside (ejecta) of the impact structure. Admixture of

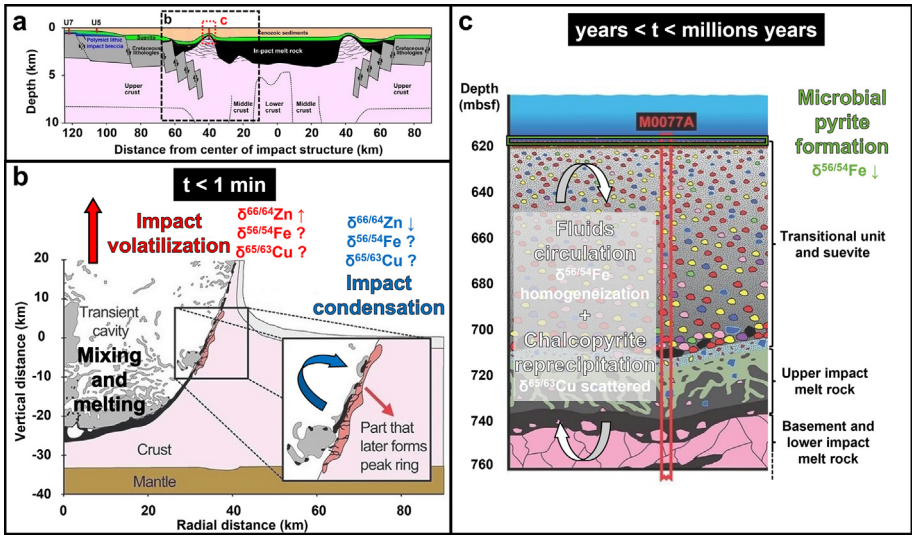


**Fig. 10.** (a) Schematic geological cross-section of the Chicxulub impact structure showing the locations of the two close-ups in (b) and (c) (adapted from Kaskes et al., 2022). (b) Schematic visualization of the Chicxulub excavation stage <1 min after the bolide impact, highlighting mixing and melting, impact volatilization, and impact condensation processes with their effect on Fe, Cu, and Zn isotope fractionation (adapted from Kaskes et al., 2022). (c) Zoomed-in snapshot of the Chicxulub peak ring location of the Hole M0077A drill core during and after the final stage highlighting microbial pyrite formation, fluids circulation, and chalcopyrite reprecipitation post-impact processes with their effect on Fe, Cu, and Zn isotope fractionation (adapted from Kaskes et al., 2022).

condensed components have previously been observed in impact-related materials (e.g., Weyrauch et al., 2019; Chernonozhkin et al., 2021). Based on Fe isotope ratio variation in microtektites from the Australasian strewn field, Chernonozhkin et al. (2021) demonstrated that the formation of these particles involves a convoluted sequence of processes that includes condensation, variable degrees of mixing between isotopically distinct reservoirs, and ablative evaporation during atmospheric re-entry. Other examples of isotopic condensation effects in natural materials include gas-associated spheroidal precipitates (GASP) formed within impact plumes on the Moon, which are found as glassy microscopic spheroids in lunar regolith breccias (Warren, 2008). Condensate glasses with structures and compositions similar to GASP have also been observed in terrestrial zhamanshinite impact glass (Gornostaeva et al., 2019).

Of the 30 K-Pg boundary sediment samples characterized by Mathur et al. (2021), only a single sample at the top of the Caribbean site (ODP Leg 165 Sample 1001A-38R 13–15 cm), displays a negative $\delta^{66/64}$Zn isotopic value ($\delta^{66/64}Zn_{JMC\text{-}Lyon}$ = −0.56‰). This value is below the typical range for sedimentary rocks and is approximated only by the two anomalous samples of UIM unit ($\delta^{66/64}$Zn of −0.12 and −0.49 for 91_1_44_46 and 93_1_19_21, respectively). The low $\delta^{66/64}$Zn value for ODP Leg 165 Sample 1001A-38R 13–15 cm has been interpreted to possibly reflect later fallout complementary to the volatilized isotopically heavy Zn reservoir (Mathur et al., 2021). Similarly, the two UIM samples from this study may reflect condensed material (Fig. 9) that is complementary to the isotopically heavy fallout material. While certainly tentative, the occurrence of this isotopically light Zn may indicate a genetic link between the UIM unit and the distally ejected material. A similar relation has previously been suggested based on major and trace element contents (de Graaff et al., 2022; Kaskes et al., 2022), and may be confirmed in the future using *in situ* isotopic proxies. If a genetic association between fallout products within and outside of the crater can be confirmed, the observed isotopic heterogeneity within the upper impact melt rock may be used to better constrain the chemical and isotopic heterogeneity in the impact plume. Although overprinted by a hydrothermal signature at the Hole M0077A drill core, combined with other isotopic systems such as Cu and Fe, the observed hints of volatilization and condensation within and outside of the Chicxulub impact structure (Figs. 9 and 10) may constrain the nature and duration of the thermal regimes active shortly after impact crater formation in the evolving impact vapor plume and ejecta curtain (Burtt et al., 2022; Morgan et al., 2022).

## 6. Conclusions

Based on their different volatility and geochemical behaviors, the use of isotope ratio data of Fe, Cu, and Zn, combined with the petrography and geochemistry of Chicxulub impactites provides evidence of large-scale post-impact hydrothermal remobilization from fluids leading to secondary alteration. All lithological units sampled by the Hole M0077A drill core appear to have been affected by an extensive hydrothermal system. Despite the widespread effects of this overprint, occurring throughout the impact structure but especially apparent in the peak ring, the Fe, Cu, and Zn isotopic systems preserve important information on the nature and extent of the complex processes taking place during and after the impact.

While the observed Fe and Cu isotopic signatures mostly reflect distinct target lithology mixing and secondary sulfide mineral formation, the Zn isotope ratios represent a powerful tool to trace some of the high-temperature processes associated with impact crater formation. The isotopic heterogeneity may be expected to be even larger at the microscale, as this study focus on bulk sample measurements. Based on our results, the stable Zn isotope ratios for the upper sections of the transitional unit and a metamorphic clast have likely retained a hint of volatility-driven isotopic fractionation. Impact volatilization has previously been observed for K-Pg boundary layer sediments around the world and similar isotopic deviations are confirmed here for the K-Pg boundary interval preserved within the materials filling up the transient cavity that formed following the Chicxulub impact event. Importantly, our data may indicate the presence of an isotopically light Zn reservoir within the upper impact melt rock unit. The isotopic signatures observed for the UIM are suggestive of (back-) condensation and may imply a genetic link between this upper impact melt rock unit and the material preserved at proximal to distal ejecta sites.

## Declaration of Competing Interest

The authors declare that they have no known competing financial interests or personal relationships that could have appeared to influence the work reported in this paper.

## Acknowledgements

The authors thank the valuable comments made by Ryan Mathur, Lucy McGee, and a third anonymous reviewer as well as associate editor Stijn Glorie that helped to improve this manuscript. We warmly thank Wendy Debouge, Sabrina Cauchies, and Jeroen de Jong for their assistance with the sample preparation and the ICP-OES, ICP-MS and MC-ICP-MS analysis at Laboratoire G-Time (Université Libre de Bruxelles). This work is supported by the Research Foundation Flanders (FWO; project G0A6517N), the Belgian Federal Science Policy Office (BELSPO; project Chicxulub), the Excellence of Science Program (EoS project ET-HoME ID 30442502), and the VUB Strategic Research Program. Pim Kaskes thanks FWO for the personal PhD fellowship awarded (projects 11E6619N, 11E6621N). Vinciane Debaille thanks the Fonds de la Recherche Scientifique (FRS-FNRS) for support. Stepan Chernonozhkin acknowledges his postdoctoral fellowship from the FWO EoS project ET-HoME. The FWO is acknowledged for providing the funding for the acquisition of the MC-ICP-MS instrumentation (ZW15-02 – G0H6216N). Frank Vanhaecke acknowledges the support from FWO under the form of the aforementioned EoS project and BOF-UGent. This study used samples provided by IODP-ICDP Expedition 364, which was jointly funded by the International Ocean Discovery Program and the International Continental Scientific Drilling Program, with contributions and logistical support from the Yucatán State Government and the National Autonomous University of Mexico.

## Appendix A. Supplementary data

Supplementary data to this article can be found online at https://doi.org/10.1016/j.gsf.2022.101410.

## References

Abramov, O., Kring, D.A., 2007. Numerical modeling of impact-induced hydrothermal activity at the Chicxulub crater. Meteorit. Planet. Sci. 42, 93–112. https://doi.org/10.1111/j.1945-5100.2007.tb00220.x.

Ackerman, L., Žák, K., Skála, R., Rejšek, J., Křížová, Š., Wimpenny, J., Magna, T., 2020. Sr-Nd-Pb isotope systematics of Australasian tektites: Implications for the nature and composition of target materials and possible volatile loss of Pb. Geochim. Cosmochim. Ac. 276, 135–150. https://doi.org/10.1016/j.gca.2020.02.025.

Barnes, S-J., 2016. Chalcophile Elements. In: White, W. (Ed.), Encyclopedia of Geochemistry. Encyclopedia of Earth Sciences Series. Springer, Cham.

Baxter, D.C., Rodushkin, I., Engström, E., Malinovsky, D., 2006. Revised exponential model for mass bias correction using an internal standard for isotope abundance ratio measurements by multi-collector inductively coupled plasma mass spectrometry. J. Anal. Atom. Spectrom. 21, 427–430. https://doi.org/10.1039/b517457k.

Bralower, T.J., Cosmidis, J., Fantle, M.S., Lowery, C.M., Passey, B.H., Gulick, S.P.S., Morgan, J.V., Vajda, V., Whalen, M.T., Wittmann, A., Artemieva, N., Farley, K., Goderis, S., Hajek, E., Heaney, P.J., Kring, D.A., Lyons, S.L., Rasmussen, C., Sibert, E., Rodriguez Tovar, F.J., Turner-Walker, G., Zachos, J.C., Carte, J., Chen, S.A., Cockell, C., Coolen, M., Freeman, K.H., Garber, J., Gonzalez, M., Gray, J.L., Grice, K., Jones, H. L., Schaefer, B., Smit, J., Tikoo, S.M., 2020. The Habitat of the Nascent Chicxulub Crater. Am. Geophys. Uni. Adv. 1. https://doi.org/10.1029/2020av000208.

Burtt, D.G., Henkes, G.A., Yancey, T.E., Schrag, D., 2022. Hot atmospheric formation of carbonate accretionary lapilli at the Cretaceous-Paleogene boundary, Brazos River, Texas, from clumped isotope thermometry. Geology 50, 636–640. https://doi.org/10.1130/G49674.1.

Chernonozhkin, S.M., González de Vega, C., Artemieva, N., Soens, B., Belza, J., Bolea-Fernandez, E., van Ginneken, M., Glass, B.P., Folco, L., Genge, M.J., Claeys, P.h., Vanhaecke, F., Goderis, S., 2021. Isotopic evolution of planetary crusts by hypervelocity impacts evidenced by Fe in microtektites. Nat. Commun. 12, 5646. https://doi.org/10.1038/s41467-021-25819-6.

Craddock, P.R., Dauphas, N., 2011. Iron and carbon isotope evidence for microbial iron respiration throughout the Archean. Earth Planet. Sci. Lett. 303, 121–132. https://doi.org/10.1016/j.epsl.2010.12.045.

Creech, J.B., Moynier, F., 2019. Tin and zinc stable isotope characterisation of chondrites and implications for early Solar System evolution. Chem. Geol. 511, 81–90. https://doi.org/10.1016/j.chemgeo.2019.02.028.

Creech, J.B., Moynier, F., Koeberl, C., 2019. Volatile loss under a diffusion-limited regime in tektites: evidence from tin stable isotopes. Chem. Geol. 528,. https://doi.org/10.1016/j.chemgeo.2019.119279 119279.

Collins, G.S., Patel, N., Davison, T.M., Rae, A.S.P., Morgan, J.V., Gulick, S.P.S., IODP-ICDP Expedition 364 Science Party, and Third-Party, I.-O.-D.-P.-, Scientists, 2020. A steeply-inclined trajectory for the Chicxulub impact. Nat. Commun. 11, 1480. https://doi.org/10.1038/s41467-020-15269-x.

Davis, A.M., Richter, F.M., 2014. Condensation and evaporation of solar system materials. Treatise Geochem. 335–360. https://doi.org/10.1016/b978-0-08-095975-7.00112-1.

de Graaff, S.J., Kaskes, P., Déhais, T., Goderis, S., Debaille, V., Ross, C.H., Gulick, S.P.S., Feignon, J.-G., Ferrière, L., Koeberl, C., Smit, J., Mattielli, N., Claeys, P.h., 2022. New insights into the formation and emplacement of impact melt rocks within the Chicxulub impact structure, following the 2016 IODP-ICDP Expedition 364. Geol. Soc. Am. Bull. 134, 293–315. https://doi.org/10.1130/B35795.1.

Dehant, V., Debaille, V., Dobos, V., Gaillard, F., Gillmann, C., Goderis, S., Grenfell, J.L., Höning, D., Javaux, E.J., Karatekin, Ö., Morbidelli, A., Noack, L., Rauer, H., Scherf, M., Spohn, T., Tackley, P., Van Hoolst, T., Wünnemann, K., 2019. Geoscience for understanding habitability in the Solar System and beyond. Space Sci. Rev. 215. https://doi.org/10.1007/s11214-019-0608-8.

Doucet, L.S., Laurent, O., Ionov, D.A., Mattielli, N., Debaille, V., Debouge, W., 2020. Archean lithospheric differentiation: Insights from Fe and Zn isotopes. Geology 48, 1028–1032. https://doi.org/10.1130/g47647.1.

Day, J.M.D., Moynier, F., Meshik, A.P., Pradivtseva, O.V., Petit, D.R., 2017. Evaporative fractionation of zinc during the first nuclear detonation. Sci. Adv. 3, e1602668.

Feignon, J.-G., de Graaff, S.J., Ferrière, L., Kaskes, P., Déhais, T., Goderis, S., Claeys, P.h., Koeberl, C., 2021. Chicxulub impact structure, IODP-ICDP Expedition 364 drill core: Geochemistry of the granite basement. Meteorit. Planet. Sci. 56, 1243–1273. https://doi.org/10.1111/maps.13705.

Feignon, J.-G., Schulz, T., Ferrière, L., Goderis, S., de Graaff, S.J., Kaskes, P., Déhais, T., Claeys, P.h., Koeberl, C., 2022. Search for a meteoritic component within the impact melt rocks of the Chicxulub impact structure peak ring, Mexico. Geochim. Cosmochim. Ac. 323, 74–101. https://doi.org/10.1016/j.gca.2022.02.006.

Goderis, S., Sato, H., Ferrière, L., Schmitz, B., Burney, D., Kaskes, P., Vellekoop, J., Wittmann, A., Claeys, Ph., de Graaff, S.J., Déhais, T., de Winter, N.J., Elfman, M., Feignon, J.-G., Ishikawa, A., Koeberl, C., Kristiansson, P., Neal, C.R., Owens, J.D., Schulz, T., Sinnesael, M., Vanhaecke, F., Van Malderen, S.J.M., Bralower, T.J., Gulick, S.P.S., Lowery, C.M., Morgan, J.V., Smit, J., Whalen, M.T., the IODP-ICDP Expedition 364 Scientists, 2021. Globally distributed iridium layer preserved within the Chicxulub impact structure. Sc. Adv. 7, eabe3647. https://doi.org/10.1126/sciadv.abe3647.

Gong, Y., Xia, Y., Huang, F., Yu, H., 2017. Average iron isotopic compositions of the upper continental crust: constrained by loess from the Chinese Loess Plateau. Ac. Geochim. 36, 125–131. https://doi.org/10.1007/s11631-016-0131-5.

González de Vega, C., Chernonozhkin, S.M., Grigoryan, R., Costas-Rodeíguez, M., Vanhaecke, F., 2020. Characterization of the new isotopic reference materials IRMM-524A and ERM-AE143 for Fe and Mg isotopic analysis of geological and biological samples. J. Anal. Atom. Spectrom. 35, 2517–2529. https://doi.org/10.1039/d0ja00225a.

Gornostaeva, T.A., Mokhov, A.V., Kartashov, P.M., Bogatikov, O.A., 2019. Comparison of the compositions and microstructures of terrestrial and Lunar impact glasses: Samples from the Zhamanshin Crater and Luna 16, 20, and 24 Missions. Petrology 27, 95–107. https://doi.org/10.1134/s0869591119010028.

Gulick, S.P.S., Barton, P.J., Christeson, G.L., Morgan, J.V., McDonald, M., Mendoza-Cervantes, K., Pearson, Z.F., Surendra, A., Urrutia-Fucugauchi, J., Vermeesch, P. M., Warner, M.R., 2008. Importance of pre-impact crustal structure for the asymmetry of the Chicxulub impact crater. Nat. Geosci. 1, 131–135. https://doi.org/10.1038/ngeo103.

Gulick, S.P.S., Bralower, T.J., Ormö, J., Hall, B., Grice, K., Schaefer, B., Lyons, S., Freeman, K.H., Morgan, J.V., Artemieva, N., Kaskes, P., de Graaff, S.J., Whalen, M. T., Collins, G.S., Tikoo, S.M., Verhagen, C., Christeson, G.L., Claeys, P.h., Coolen, M. J.L., Goderis, S., Goto, K., Grieve, R.A.F., McCall, N., Osinski, G.R., Rae, A.S.P., Riller, U., Smit, J., Vajda, V., Wittmann, A., the, Expedition, 364, Scientists, 2019. The first day of the Cenozoic. Proc. Natl. Acad. Sci. USA 116, 19342–19351. https://doi.org/10.1073/pnas.1909479116.

Hecht, L., Wittmann, A., Schmitt, R.-T., Stöffler, D., 2004. Composition of impact melt particles and the effects of post-impact alteration in suevitic rocks at the Yaxcopoil-1 drill core, Chicxulub crater, Mexico. Meteorit. Planet. Sci. 39, 1169–1186. https://doi.org/10.1111/j.1945-5100.2004.tb01135.x.

Hildebrand, A.R., Penfield, G.T., Kring, D.A., Pilkington, M., Camargo, Z., Antonio, Jacobsen, S.B., Boynton, W.V., 1991. Chicxulub Crater: A possible Cretaceous/Tertiary boundary impact crater on the Yucatán Peninsula, Mexico. Geology 19, 867–871. https://doi.org/10.1130/0091-7613(1991)019<0867:CCAPCT>2.3.CO;2.

Kamber, B.S., Schoenberg, R., 2020. Evaporative loss of moderately volatile metals from the superheated 1949 Ma Sudbury impact melt sheet inferred from stable Zn isotopes. Earth Planet. Sc. Lett. 544,. https://doi.org/10.1016/j.epsl.2020.116356 116356.

Kaskes, P., de Graaff, S.J., Feignon, J.-G., Déhais, T., Goderis, S., Ferrière, L., Koeberl, C., Smit, J., Wittmann, A., Gulick, S.P.S., Debaille, V., Mattielli, N., Claeys, P.h., 2022. Formation of the crater suevite sequence from the Chicxulub peak ring: A petrographic, geochemical, and sedimentological characterization. Geol. Soc. Am. Bull. 134, 895–927. https://doi.org/10.1130/B36020.1.

Kring, D.A., Tikoo, S.M., Schmieder, M., Riller, U., Rebolledo-Vieyra, M., Simpson, S.L., Osinski, G.R., Gattacceca, J., Wittmann, A., Verhagen, C.M., Cockell, C.S., Coolen, M.J.L., Longstaffe, F.J., Gulick, S.P.S., Morgan, J.V., Bralower, T.J., Chenot, E., Christeson, G.L., Claeys, P.h., Ferrière, L., Gebhardt, C., Goto, K., Green, S.L., Jones, H., Lofi, J., Lowery, C.M., Ocampo-Torres, R., Perez-Cruz, L., Pickersgill, A.E., Poelchau, M.H., Rae, A.S.P., Rasmussen, C., Sato, H., Smit, J., Tomioka, N., Urrutia-Fucugauchi, J., Whalen, M.T., Xiao, L., Yamaguchi, K.E., 2020. Probing the hydrothermal system of the Chicxulub impact crater. Sc. Adv. 6, eaaz3053. https://doi.org/10.1126/sciadv.aaz3053.

Kaskes, P., Déhais, T., de Graaff, S.J., Goderis, S., Claeys, P., 2021. Micro–X-ray fluorescence (μXRF) analysis of proximal impactites: High-resolution element mapping, digital image analysis, and quantifications. In: Reimold, W.U., Koeberl, C. (Eds.), Large Meteorite Impacts and Planetary Evolution VI, 550. Geological Society of America Special Paper, pp. 171–206. https://doi.org/10.1130/2021.2550(07).

Magna, T., Jiang, Y., Skála, R., Wang, K., Sossi, P.A., Žák, K., 2021. Potassium elemental and isotope constraints on the formation of tektites and element loss during impacts. Geochim. Cosmochim. Ac. 312, 321–342. https://doi.org/10.1016/j.gca.2021.07.022.

Maréchal, C.N., Nicolas, E., Douchet, C., Albarède, F., 2000. Abundance of zinc isotopes as a marine biogeochemical tracer. Geochem. Geophy. Geosyst. 1. https://doi.org/10.1029/1999GC000029.

Mathur, R., Mahan, B., Spencer, M., Godfrey, L., Landman, N., Garb, M., Pearson, D.G., Liu, S.-A., Oboh-Ikuenobe, F.E., 2021. Fingerprinting the Cretaceous-Paleogene boundary impact with Zn isotopes. Nat. Commun. 12, 4128. https://doi.org/10.1038/s41467-021-24419-8.

McDonough, W.F., Sun, S.-S., 1995. The composition of the Earth. Chem. Geol. 120, 223–253. https://doi.org/10.1016/0009-2541(94)00140-4.

Morgan, J.V., Warner, M., the Chicxulub Working Group, Brittan, J., Buffler, R., Camargo, A., Christeson, G., Denton, P., Hildebrand, A., Hobbs, R., Macintyre, H., Mackenzie, G., Maguire, P., Marin, L., Nakamura, Y., Pilkington, M., Sharpton, V., Snyder, D., Suarez, G., Trejo, A., 1997. Size and morphology of the Chicxulub impact crater. Nature 390, 472–476. https://doi.org/10.1038/37291

Morgan, J.V., Gulick, S.P.S., Bralower, T., Chenot, E., Christeson, G., Claeys, P.h., Cockell, C., Collins, G.S., Coolen, M.J.L., Ferrière, L., Gebhardt, C., Goto, K., Jones, H., Kring, D.A., Le Ber, E., Lofi, J., Long, X., Lowery, C., Mellett, C., Ocampo-Torres, R., Osinski, G.R., Perez-Cruz, L., Pickersgill, A.E., Poelchau, M.H., Rae, A.S.P., Rasmussen, C., Rebolledo-Vieyra, M., Riller, U., Sato, H., Schmitt, D.R., Smit, J., Tikoo, S., Tomioka, N., Urrutia-Fucugauchi, J., Whalen, M.T., Wittmann, A., Yamaguchi, K.E., Zylberman, W., 2016. The formation of peak rings in large impact craters. Science 354, 878–882. https://doi.org/10.1126/science.aah6561.

Morgan, J.V., Gulick, S.P.S., Mellett, C.L., Green, S.L., the Expedition 364 Scientists, 2017. Chicxulub: Drilling the K-Pg Impact Crater. Proceedings of the IODP, Volume 364: College Station, Texas. https://doi.org/10.14379/iodp.proc.364.2017

Morgan, J.V., Bralower, T.J., Brugger, J., Wünnemann, K., 2022. The Chicxulub impact and its environmental consequences. Nat. Rev. Earth Environ. https://doi.org/10.1038/s43017-022-00283-y.

Moynier, F., Beck, P., Jourdan, F., Yin, Q.-Z., Reimold, U., Koeberl, C., 2009. Isotopic fractionation of zinc in tektites. Earth Planet. Sc. Lett. 277, 482–489. https://doi.org/10.1016/j.epsl.2008.11.020.

Ni, P., Macris, C.A., Darling, E.A., Shahar, A., 2021. Evaporation-induced copper isotope fractionation: Insights from laser levitation experiments. Geochim. Cosmochim. Ac. 298, 131–148. https://doi.org/10.1016/j.gca.2021.02.007.

Osinski, G.R., Grieve, R.A.F., Hill, P.J.A., Simpson, S.L., Cockell, C., Christeson, G.L., Ebert, M., Gulick, S.P.S., Melosh, H.J., Riller, U., Tikoo, S.M., Wittmann, A., 2020. Explosive interaction of impact melt and seawater following the Chicxulub impact event. Geology 48, 108–112. https://doi.org/10.1130/G46783.1.

Petit, J.C.J., de Jong, J., Chou, L., Mattielli, N., 2008. Development of Cu and Zn isotope MC-ICP-MS measurements: application to suspended particulate matter and sediments from the Scheldt Estuary. Geostand. Geoanal. Res. 32, 149–166. https://doi.org/10.1111/j.1751-908x.2008.00867.x.

Pons, M.-L., Fujii, T., Rosing, M., Quitté, G., Télouk, P., Albarède, F., 2013. A Zn isotope perspective on the rise of continents. Geobiology 11, 201–214. https://doi.org/10.1111/gbi.12030.

Rebolledo-Vieyra, M., Urrutia-Fucugauchi, J., Marin, L.E., Trejo-Garcia, A., Sharpton, V.L., Soler-Arechalde, A.M., 2000. UNAM Scientific Shallow-Drilling Program of the Chicxulub Impact Crater. Int. Geol. Rev. 42, 928–940. https://doi.org/10.1080/00206810009465118.

Rodovská, Z., Magna, T., Žák, K., Skála, R., Brachaniec, T., Visscher, C., 2016. The fate of moderately volatile elements in impact events – Lithium connection between the Ries sediments and central European tektites. Meteorit. Planet. Sci. 51, 2403–2415. https://doi.org/10.1111/maps.12733.

Rodovská, Z., Magna, T., Žák, K., Kato, C., Savage, P.S., Moynier, F., Skála, R., Ježek, J., 2017. Implications for behavior of volatile elements during impacts – Zinc and copper systematics in sediments from the Ries impact structure and central European tektites. Meteorit. Planet. Sci. 52, 2178–2192. https://doi.org/10.1111/maps.12922.

Rouxel, O., Fouquet, Y., Ludden, J.N., 2004. Copper isotope systematics of the Lucky Strike, Rainbow, and Logatchev Sea-Floor Hydrothermal Fields on the Mid-Atlantic Ridge. Econ. Geol. 99, 585–600. https://doi.org/10.2113/gsecongeo.99.3.585.

Rudnick, R.L., Gao, S., 2003. 3.01 – Composition of the Continental Crust. In: Holland, H.D., Turekian, K.K. (Eds.), Treatise on Geochemistry 3, 1–64. https://doi.org/10.1016/b0-08-043751-6/03016-4.

Schmitz, B., Andersson, P., Dahl, J., 1988. Iridium, sulfur isotopes and rare earth elements in the Cretaceous-Tertiary boundary clay at Stevns Klint, Denmark. Geochim. Cosmochim. Ac. 52, 229–236. https://doi.org/10.1016/0016-7037(88)90072-5.

Schulte, P., Alegret, L., Arenillas, I., Arz, J.A., Barton, P.J., Bown, P.R., Bralower, T.J., Christeson, G.L., Claeys, P.h., Cockell, C.S., Collins, G.S., Deutsch, A., Goldin, T.J., Goto, K., Grajales-Nishimura, J.M., Grieve, R.A.F., Gulick, S.P.S., Johnson, K.R., Kiessling, W., Koeberl, C., Kring, D.A., MacLeod, K.G., Matsui, T., Melosh, J., Montanari, A., Morgan, J.V., Neal, C.R., Nichols, D.J., Norris, R.D., Pierazzo, E., Ravizza, G., Rebolledo-Vieja, M., Reimold, W.U., Robin, E., Salge, T., Speijer, R.P., Sweet, A.R., Urrutia-Fucugauchi, J., Vajda, V., Whalen, M.T., Willumsen, P.S., 2010. The Chicxulub asteroid impact and mass extinction at the Cretaceous-Paleogene boundary. Science 327, 1214–1218. https://doi.org/10.1126/science.1177265.

Simpson, S.L., Osinski, G.R., Longstaffe, F.J., Schmieder, M., Kring, D.A., 2020. Hydrothermal alteration associated with the Chicxulub impact crater upper peak-ring breccias. Earth Planet. Sc. Lett. 547,. https://doi.org/10.1016/j.epsl.2020.116425 116425.

Smit, J., 1999. The global stratigraphy of the Cretaceous-Tertiary boundary impact ejecta. Annu. Rev. Earth Pl. Sc. 27, 75–113. https://doi.org/10.1146/annurev.earth.27.1.75.

Sprain, C.J., Renne, P.R., Clemens, W.A., Wilson, G.P., 2018. Calibration of chron C29r: New high-precision geochronologic and paleomagnetic constraints from the Hell Creek region, Montana. Geol. Soc. Am. Bull. 130, 1615–1644. https://doi.org/10.1130/B31890.1.

Stöffler, D., Grieve, R.A.F., 2007. Impactites, ch 2.11. In: Fettes, D., Desmons, J. (Eds.), Metamorphic Rocks: A Classification and Glossary of Terms, Recommendations of the International Union of Geologic. Cambridge University Press, Cambridge.

Swisher, C.C., Grajales-Nishimura, J.M., Montanari, A., Margolis, S.V., Claeys, P.h., Alvarez, W., Renne, P., Cedillo-Pardoa, E., Maurrasse, F.-J.-M.-R., Curtis, G.H., Smit, J., McWilliams, M.O., 1992. Coeval $^{40}Ar/^{39}Ar$ Ages of 65.0 million years ago from Chicxulub crater melt rock and Cretaceous-Tertiary boundary tektites. Science 257, 954–958. https://doi.org/10.1126/science.257.5072.954.

Tuchscherer, M.G., Reimold, W.U., Gibson, R.L., de Bruin, D., Späth, A., 2006. Major and trace element compositions of melt particles and associated phases from the Yaxcopoil-1 drill core, Chicxulub impact structure, Mexico. Meteorit. Planet. Sci. 41, 1361–1379. https://doi.org/10.1111/j.1945-5100.2006.tb00527.x.

Urrutia-Fucugauchi, J., Marin, L., Trejo-Garcia, A., 1996. UNAM scientific drilling program of Chicxulub impact structure-Evidence for a 300 kilometer crater diameter. Geophys. Res. Lett. 23, 1565–1568. https://doi.org/10.1029/96gl01566.

Urrutia-Fucugauchi, J., Chavez-Aguirre, J.M., Pérez-Cruz, L., De la Rosa, J.L., 2008. Impact ejecta and carbonate sequence in the eastern sector of the Chicxulub crater. C. R. Geosci. 340, 801–810. https://doi.org/10.1016/j.crte.2008.09.001.

Urrutia-Fucugauchi, J., Pérez-Cruz, L., Campos-Arriola, S.E., Escobar-Sánchez, E., Velasco-Villarreal, M., 2014. Magnetic susceptibility logging of Chicxulub proximal impact breccias in the Santa Elena borehole: implications for emplacement mode. Stud. Geophys. Geod. 58, 100–120. https://doi.org/10.1007/s11200-013-0803-0.

Warren, P.H., 2008. Lunar rock-rain: Diverse silicate impact-vapor condensates in an Apollo-14 regolith breccia. Geochim. Cosmochim. Ac. 72, 3562–3585. https://doi.org/10.1016/j.gca.2008.04.031.

Weyrauch, M., Zipfel, J., Weyer, S., 2019. Origin of metal from CB chondrites in an impact plume - A combined study of Fe and Ni isotope composition and trace element abundances. Geochim. Cosmochim. Ac. 246, 123–137. https://doi.org/10.1016/j.gca.2018.11.022.

Whalen, M.T., Gulick, S.P.S., Lowery, C.M., Bralower, T.J., Morgan, J.V., Grice, K., Schaefer, B., Smit, J., Ormö, J., Wittmann, A., Kring, D.A., Lyon, S., Goderis, S., the, IODP-ICDP, Epedition, 34, Scientists, 2020. Winding down the Chicxulub impact: The transition between impact and normal marine sedimentation near ground zero. Mar. Geol. 430,. https://doi.org/10.1016/j.margeo.2020.106368 106368.

Wimpenny, J., Marks, N., Knight, K., Rolison, J.M., Borg, L., Eppich, G., Badro, J., Ryerson, F.J., Sanborn, M., Huyskens, M.H., Yin, Q.-z., 2019. Experimental determination of Zn isotope fractionation during evaporative loss at extreme temperatures. Geochim. Cosmochim. Ac. 259, 391–411. https://doi.org/10.1016/j.gca.2019.06.016.

Wood, B.J., Smythe, D.J., Harrison, T., 2019. The condensation temperatures of the elements: A reappraisal. Am. Mineral. 104, 844–856. https://doi.org/10.2138/am-2019-6852ccby.

Zhu, X.K., O'Nions, R.K., Guo, Y., Belshaw, N.S., Rickard, D., 2000. Determination of natural Cu-isotope variation by plasma-source mass spectrometry: implications for use as geochemical tracers. Chem. Geol. 163, 139–149. https://doi.org/10.1016/S0009-2541(99)00076-5.

Zürcher, L., Kring, D.A., 2004. Hydrothermal alteration in the core of the Yaxcopoil-1 borehole, Chicxulub impact structure, Mexico. Meteorit. Planet. Sci. 39, 1199–1221. https://doi.org/10.1111/j.1945-5100.2004.tb01137.x.